The International Journal of Advanced Manufacturing Technology (2026) 145:269–293
https://doi.org/10.1007/s00170-026-18372-3

ORIGINAL ARTICLE

Laser cutting of simple and complex geometries in structural steel: toward fabrication of metastructures

Hasan N. Olmez[1] · Tugberk Guner[1] · Gabriele Zanon[1] · Marco Brugnolli[2] · Oreste S. Bursi[1]

Received: 18 February 2026 / Accepted: 19 May 2026 / Published online: 25 May 2026

Abstract

Fiber laser cutting (LC) plays a crucial role in modern industrial manufacturing, offering rapid and precise machining, together with the ability to produce complex geometries that are otherwise difficult to fabricate. However, LC inherently involves complex thermo–mechanical interactions, localized heating, rapid cooling, and residual stress formation that can alter microstructures, modify material properties, and influence long-term structural performance. This study presents a comprehensive experimental investigation of fiber LC of S235 structural steel, focusing on how assist-gas type, process parameters, and geometry complexity affect cut-surface quality, thermal response, and residual stress development. Cutting trials on both straight and complex geometries were performed with oxygen, nitrogen, and compressed air as assist gases. The quality of the cuts was evaluated through visual inspection and measurements of roughness, perpendicularity, and hardness. In addition, the thermal effects and residual stresses in straight LC samples were examined using infrared camera imaging and X-ray diffraction techniques. In terms of LC of complex geometries, circular and curved features, sharp corners, closely spaced cuts, and auxetic and architected metastructural patterns were investigated. LC-assisted by air has shown superior performance compared to nitrogen- and oxygen-assisted LC in the production of small-scale features and geometries critical for metastructure fabrication. These findings underscore the significant impact of assist-gas choice on post- LC surface quality and manufacturability. Laser cutting has been illustrated as a reliable method for fabricating steel-based metastructures, wherein the geometric precision and resolution of thin features are essential for both structural integrity and functional performance.

Keywords Laser cutting · Metastructures · Infrared thermography · X-ray diffraction · Auxetic

1 Introduction

1.1 Background and motivation

The rapid evolution of laser cutting (LC) technology is activated by advances in control systems, such as CNC, and breakthroughs in laser science, including beam generation and focus innovations. These improvements have improved cutting precision, operational speed, and reliability, making LC an critical technique for modern manufacturing [1, 2]. Among the various LC methods, fiber lasers stand out for their efficiency and effectiveness, specifically in the processing of structural steel for critical applications in the construction sector [3]. Their advantages in steel structures include the ability to use the same machine for both holes and straight cuts, thereby reducing the time and costs. In general, LC offers multiple benefits: high accuracy and speed, low cost, repeatable precision, superior cutting-edge quality, minimal material waste, and elimination of several intermediate steps compared with mechanical and thermal alternatives such as blanking, drilling, oxyfuel, and plasma [4]. Consequently, LC is particularly advantageous for handling intricate geometries, such as circular hollow sections, where precision is essential to avoid increased assembly costs [5, 6].

Since the introduction of EN 1090-1 [7], which sets the requirements for structural components through execution

✉ Tugberk Guner
tugberk.guner@unitn.it

1 Department of Civil, Environmental, and Mechanical Engineering, University of Trento, Via Mesiano, 77, Trento 38123, TN, Italy

2 Adige-Sys, BLM Group, Levico Terme, Trento 38056, TN, Italy

classes (EXC), increasingly stringent standards have been applied to steel structures. Together with EN 1090-2 [8], these standards define the quality assessments required for both the thermal and mechanical processes, including LC, which are applicable to all EXCs. Importantly, LC-fabricated elements strongly affect the performance of a system under operational and extreme loads such as snow or wind on roofs or high-cycle fatigue on bridges and footbridges [9]. The efficiency of LC depends on process parameters such as speed, power, and gas pressure, which in turn influence the heat-affected zone (HAZ), surface quality, and residual stresses near the cut edge [10–12]. Optimal parameter selection yields narrow kerfs and high-quality edges, which are critical for structural applications [12, 13]. The HAZ, defined as the region of microstructural change measured perpendicular to the cut edge, is of particular concern due to the potential for local degradation and embrittlement. Rapid heating and cooling typically harden the HAZ, transforming the ferritic structures into fine pearlite and martensite, similar to quenched microstructures [14, 15]. Comparative investigations of thermal and mechanical cutting on structural steels have also confirmed pronounced hardness gradients at cut edges, with laser- and plasma-cut, emphasize the sensitivity of HAZs to process conditions [16]. In addition, LC inevitably introduces residual stresses: while compressive stresses outside the HAZ may be beneficial, tensile stresses within the HAZ combined with external loads reduce the fatigue strength [17, 18].

Surface integrity is crucial for the functional performance of machined metal components and influences their fatigue life, corrosion resistance, and durability [19, 20]. In LC, the cut-front temperature directly affects kerf quality, and precise thermal management has been shown to improve the dimensional accuracy and surface finish, as demonstrated for aluminum alloys [21]. Therefore, monitoring the temperature during LC plays a decisive role in the cut quality [22]. Real-time monitoring enables the dynamic adjustment of parameters to maintain optimal conditions. For instance, Dubey et al. [23] demonstrated that the optical and thermal properties of materials strongly affect LC performance and that continuous monitoring can improve results by adapting to local variations. Miraoui et al. [24] further reported that parameter variations significantly alter microhardness and microstructure, underscoring the importance of optimization. Studies on CO_2 LC of structural steels such as 4130 have also highlighted the need for parameter optimization to ensure superior cut quality with minimal thermal damage [25]. Predictive models have been developed for dimensional tolerances in LC, improving the geometric accuracy in thin mild steel plates and emphasizing the need for reliable process modeling in precision manufacturing [26]. Recent comprehensive review of Nabavi et al. [27] for LC process modelling have highlighted the multidimensional nature of kerf formation, demonstrating geometrical and mechanical accuracy, metallurgical transformation, and defect formation must be considered together when predicting cut quality and surface integrity.

Building upon these capabilities, LC have advanced beyond the fabrication of simple structural elements. High-strength lattice structures, metamaterials, and metastructures—finite architected assemblies derived from unit cells—can be produced to reduce weight while maintaining strength [28]. Flat-sheet fiber LC is particularly suited for their manufacture, as it provides micrometric kerf control, repeatable thin ligaments, and scalable production of large panels that can be folded, joined, or laminated in 3D layouts [29]. Recent studies have demonstrated the LC of auxetic and chiral patterns [30] and the manufacturing of auxetic tubular structures with improved impact resistance [31, 32]. Precision LC also enables the integration of microstructural features with multimaterial composites, allowing the fabrication of stress-optimized geometries with enhanced toughness or bonding performance [33]. Moreover, the combination of LC with additive manufacturing has opened new opportunities: 3D LC combined with AM can produce parts with complex internal features [34], enabling adaptive structures with foldable elements suitable for deployable and transportable applications in space, aerospace, automotive, and structural engineering [35]. However, these opportunities are highly sensitive to parameter selection (power–speed–focus–gas), requiring careful optimization to ensure reliable quality [4].

Classical investigations in the manufacturing-process literature further elucidate these sensitivities. In particular, Chen et al. [36] demonstrated that assist-gas jet dynamics—pressure, nozzle geometry, and standoff distance—govern kerf formation, dross removal, and surface oxidation during LC of steels, directly influencing edge morphology and HAZ thickness. Complementarily, Thomas [37] quantified how traverse-speed variations alter the microstructure and fatigue performance of laser-cut edges in structural steels, linking process control to long-term durability. These findings highlight that achieving defect-free and dimensionally accurate features in architected or metastructural designs requires not only geometric precision but also a deep understanding of gas-flow and thermal-cycle interactions during LC.

While these studies provide valuable insight into laser cut quality, thermal effects, and microstructure, few investigations address complex, fine-featured geometries under realistic industrial conditions, combining surface quality, residual stress, and manufacturability assessments. This gap motivates the present work, and accordingly, the novelty of this work lies in its industrially relevant integration of manufacturability, surface integrity assessment, and residual stress characterization for fiber LC of structural steel across both simple and highly complex geometries. Unlike most existing LC studies, which often focus on laboratory-scale parameter optimisation, isolated quality metrics, or microstructural analysis of straight cuts, we combined infrared thermography and X-ray diffraction (XRD) with detailed surface quality, hardness, and geometric-fidelity assessments to demonstrate explicit links between assist-gas selection, thermal fields, residual stress development, and manufacturability. In particular, the work provides one of the first systematic experimental evaluations of LC applied to fine-featured metastructural and auxetic steel patterns under industrially suggested and common used cutting conditions, revealing practical limits and geometry-specific constraints that cannot be captured by conventional studies focusing on straight cuts. By documenting representative best-practice industrial configurations rather than idealised optimisation cases, the study delivers new, practically actionable insight into how laser–material–gas interactions govern the feasibility and structural reliability of complex laser cut steel metastructures.

1.2 Scope

The aim of this study is to identify the limitations and opportunities of fiber LC for structural steel elements by investigating fabricated and machined members, with a particular focus on straight and complex cutting patterns, including sharp corners, curved features, and closely spaced parallel passes. Complementarily, the feasibility of producing non-conventional design topologies—such as auxetic, chiral, and other architected metastructural patterns—was explored, and their manufacturability using advanced LC was critically assessed. A key aspect of this study is the elucidation of the effects of LC process parameters, with particular emphasis on the role of the assist-gas type on the quality, dimensional precision, and post-processing requirement of the resultant steel structures. Although modern LC systems are renowned for their capability to produce highly intricate geometries in steel sheets and tubular members, concerns remain regarding the structural integrity of the fabricated parts, dimensional deviations from nominal design, surface quality and cleanness, as well as the extent of secondary finishing or post-processing required—factors that critically influence large-scale industrial adoption and real-world structural applications. By addressing these challenges, this research provides foundational insights into the interplay between LC parameters and complex design outcomes, thereby advancing practical knowledge and supporting the integration of LC in novel structural and metastructural applications.

In line with this objective, the first phase of this study focused on straight cuts, where the effects of LC and its parameters were evaluated with respect to key quality and performance indicators for structural steel members. Specifically, i) the quality of the laser-cut surface, assessed through visual inspection and quantitative roughness, hardness, and perpendicularity profiling; ii) the thermal effects during and after LC; and iii) the distribution of residual stresses were investigated. Compared with the current literature, this study extends the experimental design space and provides new reference data for structural applications. In the second phase, the investigation was extended to complex geometries and innovative cutting patterns, where the evaluation relied on detailed visual inspection, supplemented by dimensional accuracy checks, to capture manufacturability challenges and defect formation mechanisms.

In summary, the paper is organized as follows. Section 2 introduces the fundamentals of the LC process considered in this study and describes the selected range of processing parameters, methodology, and experimental setup. Section 3 reports the experimental findings for straight cuts, including assessments of cut; surface quality, thermal field measurements, and residual stress distributions. Section 4 expands the investigation to complex cutting patterns—covering sharp corners, curved profiles, narrowly spaced parallel cuts, and dense geometrical configurations—and discusses their manufacturability and practical feasibility. In addition, the appendix provides details on the emissivity calibration of S235 structural steel.

2 Description of laser cutting technologies and experimental setup

LC was performed using an industrial LS7 fiber LC machine manufactured by the BLM Group, capable of reaching a peak laser power of 20 kW and a cutting speed of 140 m/min. The employed laser source was an nLight CFL-4000 operating in continuous and pulsed modes with a near-Gaussian beam profile. Beam quality was characterized by a beam parameter product (BPP) below 2.8 mm mrad, delivered through an optical fiber with a 50 μm core diameter. The beam was delivered to the cutting head and focused onto the workpiece using a standard industrial optic. The focus position relative to the plate surface varied with the cutting condition and is reported for each experimental group in Tables 2 and 4, where selected offsets ensured stable kerf formation and efficient melt ejection.

Assist gas was supplied through a standard industrial coaxial cutting nozzle integrated into the LC head. The nozzle diameter and stand-off distance were selected according to the cutting configuration and material thickness and are explicitly reported for each experimental group in Table 2 and 4. This nozzle arrangement ensured axisymmetric gas flow around the laser beam, promoting stable melt expulsion and consistent kerf formation. It must be noted that the assist gases (O_2, N_2, and compressed air) were supplied through standard industrial gas lines integrated into the LC system and correspond to commercially available industrial-grade gases, representative of typical structural steel LC practice.

The cuts were made on rolled S235 steel sheets with thicknesses of 6 and 12 mm. The technical details provided by the manufacturer for the sheets are listed in Table 1 along with their chemical and mechanical properties.

2.1 Experimental setup

The LS7 LC machine used in this study allows for comprehensive control over a wide range of parameters, including laser power, duty cycle, cutting speed, nozzle diameter, focus position, assist gas type (O_2, N_2, or compressed air), and gas pressure. Although the LC7 is capable of reaching a peak power of 20 kW, the maximum power applied in this study was limited to 12 kW due to safety constraints associated with the cutting of 12 mm thick steel.

To investigate the influence of LC parameters, straight cuts were examined in detail, and later, complex geometries combining curved cuts, discontinuous paths, sharp corners, closely spaced parallel cuts (which may lead to thermal overlap), and metastructural patterns were also analyzed.

It should be noted that the experimental configurations investigated in this study do not follow a strict one-factor-at-a-time design. Instead, each parameter set represents a practically optimized cutting configuration commonly employed in industry, selected to ensure stable operation and favorable surface integrity for the corresponding cutting modes. Consequently, the results were interpreted in a comparative sense, reflecting the coupled effects governing cut quality under realistic manufacturing conditions.

The quality and roughness of the cut surface were evaluated using a KEYENCE VHX-7000 digital microscope. The magnification settings were aligned with those used in the Miyotoyo surface roughness tester. Following calibration with a reference sample, measurements were made at a magnification of 80x, using cutoff wavelengths of 8 µm for λ_s and 2.5 mm for λ_c. The surface roughness assessment adhered to ISO 9013 [38] and EN 1090-2 [8] standards, with measurements taken after the initial 15 mm of the cut. Ten measurement lines were positioned close to both the lower and upper edges of the cut, where the thermal effects were most evident. The microscope was also used to capture detailed images of the cut surfaces; where images were taken at a magnification of 20x and 80x.

2.2 Thermal measurements

The thermal effects induced by LC are important for the performance of structural components, as the rapid thermal cycles associated with the process can substantially modify material properties and undermine structural integrity. The HAZ frequently exhibits notable changes in its microstructure, such as grain enlargement and phase shifts, which can lead to imperfections such as microcracks, dross accumulation, or uneven edges. In addition, thermal cycling can induce residual stresses, dimensional distortions, and alterations in hardness, fatigue resistance, and corrosion behavior. For instance, the formation of brittle martensitic phases in steel can reduce the structural durability, whereas grain coarsening within the HAZ may adversely affect the fatigue life [39].

The temperature distribution during both the cutting and cooling phases was measured using an Optris 400 infrared (IR) camera. This instrument operates within a temperature range of 0-250°C and records data at a frequency of 27 Hz. The experimental setup for temperature measurement is shown in Fig. 1.

The IR camera enables real-time monitoring of the steel surface and its temperature profile, allowing accurate identification of the location and timing of the initial spall event. A key aspect of IR thermography is the calibration of emissivity, which is not an intrinsic material property. For steel, emissivity depends on surface characteristics (e.g., color, texture, and grain size) and process conditions such as radiation wavelength, surface temperature, observation angle, and environmental factors [40]. Accordingly, a detailed emissivity calibration procedure was conducted, as described in Appendix A.

Table 1 Chemical composition and mechanical–physical properties of S235 steel sheets

Chemical composition (%)								
C	Mn	Si	P	S	Al	Cu	Cr	Mo
0.039	0.456	0.025	0.005	0.001	0.032	0.144	0.025	0.008
Mechanical and physical properties								
Yield strength [MPa]	Tensile strength [MPa]	Elongation [%]	Thermal conductivity [W/mK]	Specific heat [J/kgK]	Linear thermal exp. coeff. [1/K]			
307	398	27.9	63	420	1.05×10^{-5}			

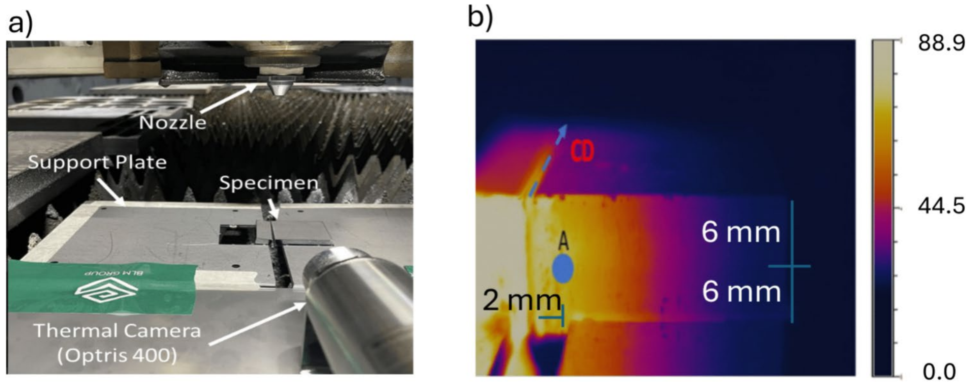

Fig. 1 The LC and temperature monitoring for a straight cut: (**a**) setup; (**b**) thermography made after 30 s LC for a thickness value of 12 mm (CD: cutting direction)

2.3 Residual stress measurements

Residual stress is a critical factor that affects the fatigue resistance and long-term structural performance of LC components. Residual stress measurements were conducted using X-ray diffraction (XRD). Specimens chosen for XRD analysis underwent annealing within the range of 450–650° C, followed by slow cooling to relieve preexisting stresses and establish a stress-free reference state prior to LC.

X-ray Residual Stress Analysis (XRSA) was conducted using a Panalytical X'Pert MRD instrument, applying the $sin^2\psi$ *method* [41] and Co Kα radiation. The measurements were performed at three distinct rotation angles: 0° , 45°, and 90°. The cut surface and each stage of layer removal were analyzed using standard XRD patterns. Data collection was carried out on a Thermo Xtra 120 diffractometer utilizing Mo Kα radiation across a 2θ range of 16.5°–66.0°. A sampling increment of 0.025° and a counting time of 20 s were employed. Potential sources of measurement uncertainty, such as surface preparation, coarse grains, stress gradients with depth, and instrument alignment, were identified and addressed in accordance with established standards, such as ASTM E2860 and ASTM E915 [42, 43].

Whole powder pattern modeling [44] was used to analyze the XRD data. This approach facilitated the estimation of the average size of the crystalline domains and the identification of inhomogeneous strain by examining the width and shape of the diffraction peak profiles.

3 Straight cuts

Specimens with dimensions of 45 mm × 35 mm were prepared from steel sheets of 6 mm and 12 mm thickness and subsequently processed using LC with the parameters specified in Table 2. Compressed-air-assisted cutting was not included herein, as O_2- and N_2-assisted cutting are the most commonly employed assist-gas configurations in industry and found to be superior. Accordingly, the straight-cut study focuses on these two gases to establish representative upper-bound performance trends. The influence of compressed air is examined in Chapter 4, where its role becomes more relevant for complex cutting paths and manufacturability considerations. The cutting parameters reported in Table 2 do not result from a formal parametric optimisation study; instead, each parameter set represents an expert-validated, industrially optimised cutting configuration commonly employed for LC of structural steels, selected to ensure stable operation, reliable penetration, and acceptable surface quality for the corresponding assist-gas type and operating mode.

Table 2 Laser cutting parameters for Straight Cuts (SC) and Circular Cuts (CC)

#	Thick. [mm]	Power [kW]	Duty-cycle [%]	Mode	Freq. [Hz]	Veloc. [mm/min]	Nozzle Dia. [mm]	S-off [mm]	Focus [mm]	Gas Type	Pres. [bar]
CC1/SC1	12	6	–	Cont.	–	1800	1.2	1	+6	O_2	0.8
CC2/SC2	12	12	–	Cont.	–	900	1.5	0.5	+10	O_2	0.5
CC3/SC3	12	4.5	25	Pul.	10	180	1.2	1	+6	O_2	0.8
CC4/SC4	12	12	–	Cont.	–	4300	7	0.3	-1	N_2	6.0
SC5	6	4.7	–	Cont.	–	3200	1.2	0.7	+6	O_2	0.7
SC6	6	3	25	Pul.	50	400	1.2	1	+3	O_2	0.5
SC7	6	6	–	Cont.	–	6500	5	0.5	-3	N_2	10
SC8	6	12	–	Cont.	–	14000	5	0.5	-4	N_2	7.5

3.1 Quality of the cut surface

The quality of the cut surface directly affects structural integrity, performance, and manufacturability. Smooth and precise cuts reduce stress concentrations, enhance fatigue resistance, and improve dimensional accuracy, thereby minimizing the need for post-processing. As discussed in Section 4, this is particularly important for maintaining the geometric and functional integrity of intricate patterns. Accordingly, the cut surfaces obtained from straight LC were evaluated using the microscope images shown in Figs. 2 and 3, and the following conclusions were drawn:

- For O_2-assisted cuts, high power (12 kW) combined with slower cutting speeds (900mm/min) produced more uniform striations, whereas lower power (6 kW) led to irregular striations near the lower edge. Conversely,

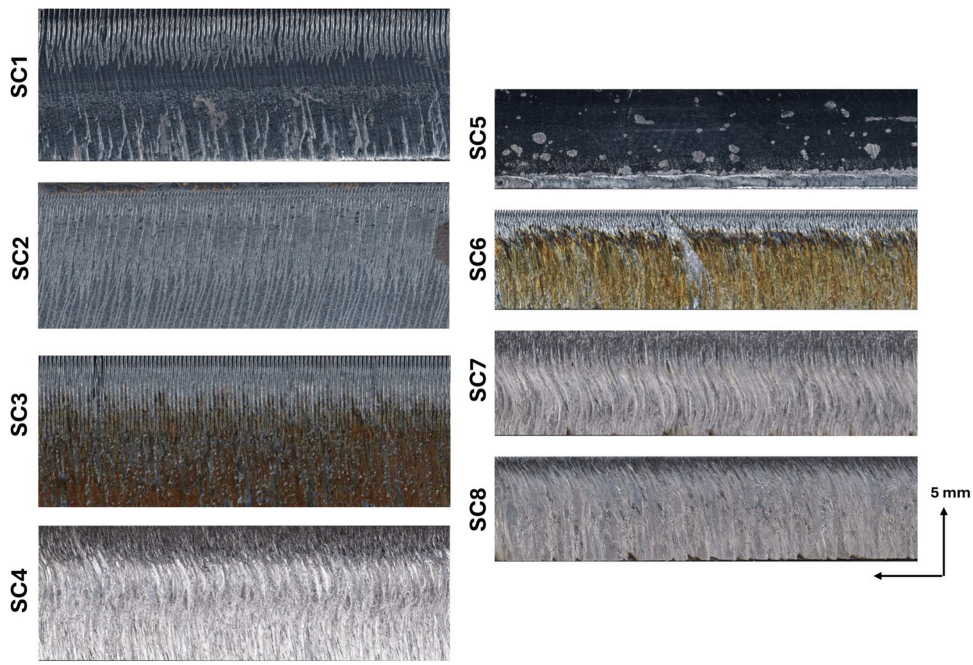

Fig. 2 Microscope images of cutting surfaces with a magnification factor of 20x

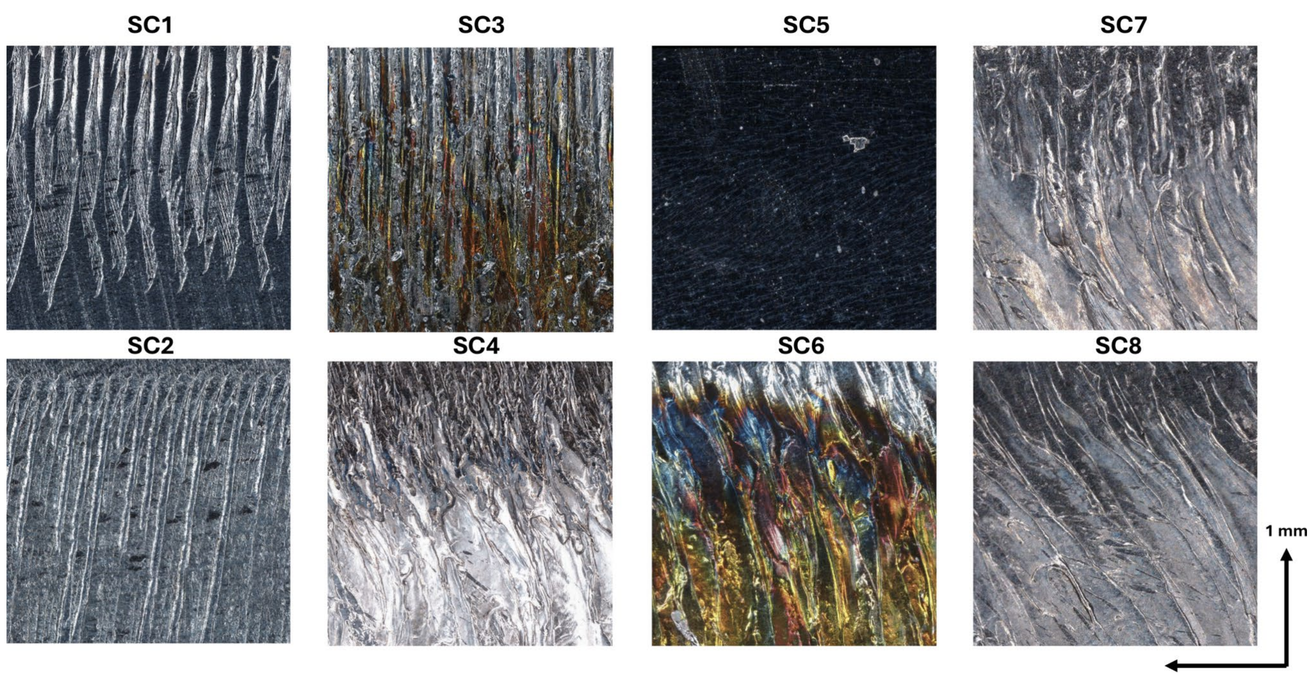

Fig. 3 Microscope images of the top side of cutting surfaces with a magnification factor of 80x

excessive power occasionally results in a rougher surface finish near the bottom region.

- Cutting with O_2 in pulsed mode, i.e. SC3 generated multiple vertical indentations extending from the top to the bottom surface for both material thicknesses.
- In general, O_2-assisted cuts performed at reduced cutting speeds (900 mm/min) showed noticeable oxidation on the cut surfaces. This suggests prolonged interaction between the molten material and the reactive assist gas.
- Use of N_2 as the assist gas enabled significantly higher cutting speeds (up to 14,000 mm/min); however, fine micro-striations were still observed extending from the top to the bottom of the cut edges.
- The visually optimal surface quality was obtained for sample SC5 (6 mm thickness) using O_2 at low power (4.7 kW) and moderate speed (3200 mm/min), yielding a smooth and uniform cut profile.
- Samples cut with O_2 (SC1–SC3) exhibited comparatively higher oxidation and surface roughness due to the exothermic oxidation process.
- The O_2 pulsed mode samples (SC3 and SC6) displayed periodic melting patterns, attributed to repeated localized heating and oxidation cycles during the pulse intervals.
- Thicker specimens (12 mm) generally exhibited more pronounced striations, while thinner samples demonstrated smoother cut surfaces and improved edge morphology.
- Microscopic observations showed that oxidation in O_2-assisted cuts was more pronounced near the lower edge, where reduced melt ejection and longer interaction time favored oxide formation.
- N_2-assisted cuts (SC4, SC7, SC8) showed minimal discoloration and a metallic surface appearance, reflecting the absence of oxidation under an inert assist-gas atmosphere.

Quantifiable indicators of the quality of cut surfaces include surface roughness, perpendicularity, and hardness, all of which have been demonstrated to have a direct correlation with fatigue life, load-bearing capacity, and resistance to wear and corrosion [45]. Specifically, smooth surfaces, characterized by lower surface roughness, are advantageous for reducing stress concentrations, enhancing weldability, and minimizing the necessity for post-processing [46]. Furthermore, perpendicularity is important in assemblies to ensure precision in fitting, equitable load distribution, and proper alignment.

Herein, assessments of surface roughness, perpendicularity, and hardness were performed on the cut surfaces of straight LC tests in accordance with the established standards [8]. The code threshold table stipulates the permissible limits for surface roughness and perpendicularity based on material thickness, thereby ensuring adherence to the established manufacturing standards (Refer to Table 3). The threshold for hardness in the HV10 test was set at 450 μm , guaranteeing the material's resistance to indentation and confirming its appropriateness for structural applications [47]. The assessment of perpendicularity involved measuring the gap between the upper and lower surfaces within a defined range, requiring the removal of 0.6 mm to 1 mm, depending on the thickness values.

The results are shown in Fig. 4 and the following observations were made.

- An increase in specimen thickness (i.e., 6 to 12mmm) was associated with a notable rise in surface roughness values, indicating a stronger influence of material thickness on the quality of the cut edge.
- For both thicknesses, LC operations employing high-velocity $N_2 \geq$ (6500 mm/min) or pulsed-mode O_2 (SC3) resulted in elevated average surface roughness and greater variability, suggesting less stable melt expulsion and thermal interaction during these conditions.
- Although the low-power, medium-speed O_2-assisted cut (SC1, 6 kW, 1800mm/min) yielded favourable results in terms of reduced surface roughness, it exhibited a significantly higher deviation (≈ 0.44) from perpendicularity compared to the other cutting conditions (≤ 0.23), indicating a trade-off between edge quality and geometrical accuracy.
- Regarding hardness, the most desirable result was obtained under low-velocity N_2 conditions (4300 mm/min), SC4, attributed to the lower thermal influence on the cut surface for thickness of 12 mm. Conversely, higher-velocity N_2-assisted cutting (14000 mm/min), SC8, led to greater variability in hardness for thickness of 6 mm, suggesting an increased sensitivity of the surface properties to rapid cooling and localized thermal gradients.

3.2 Thermal effects

LC parameters strongly influence the thermal distribution within the substrate. The thermal profile during straight LC

Table 3 Surface roughness ranges and perpendicularity/angularity tolerances (*a*: thickness of steel in mm)

Range	R_{z5} [μm]	Range	Perpendicularity [mm]
1	$10 + (0.6\,a)$	1	$0.05 + 0.003\,a$
2	$40 + (0.8\,a)$	2	$0.15 + 0.007\,a$
3	$70 + (1.2\,a)$	3	$0.4 + 0.01\,a$
4	$110 + (1.8\,a)$	4	$0.8 + 0.02\,a$
		5	$1.2 + 0.035\,a$

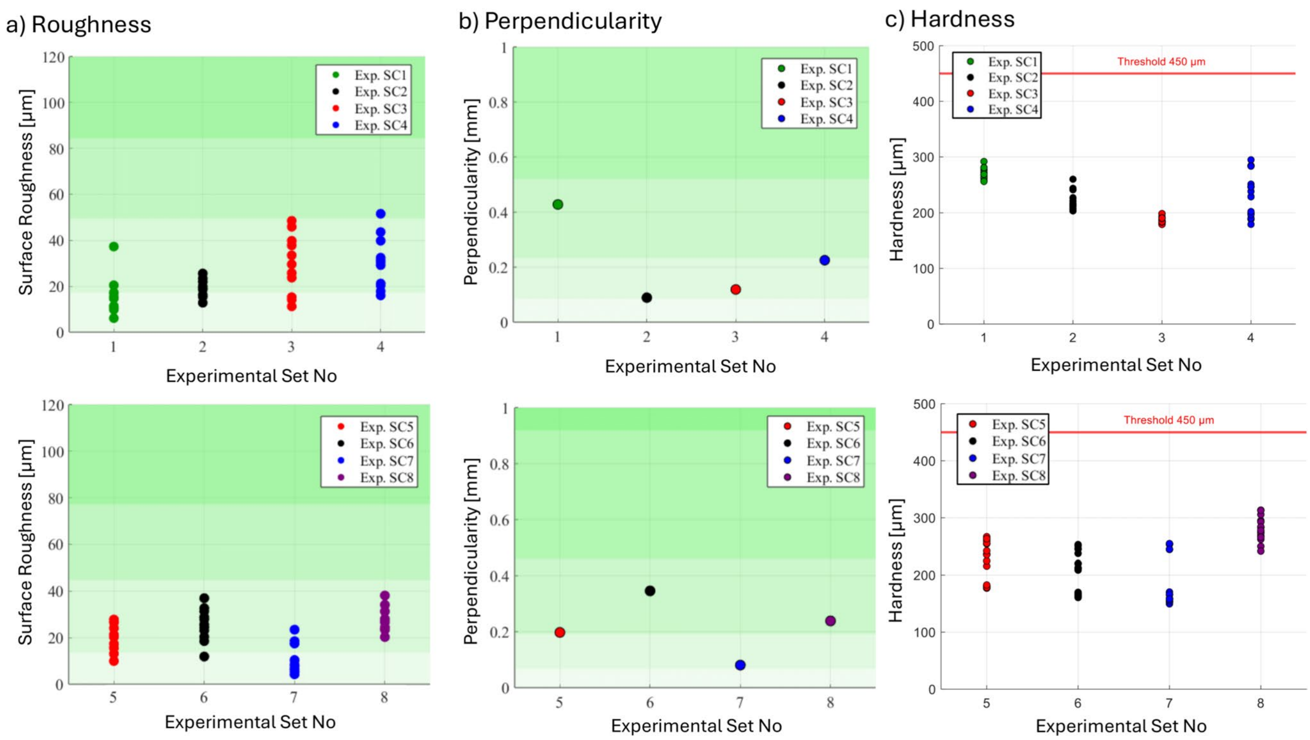

Fig. 4 Quality measurements for straight cut with the thickness of 12 and 6 mm (the gradients of green represent the ranges provided in Table 3)

was measured, and the corresponding temperature histories are presented in Fig. 5. Temperature data were acquired at the mid-thickness locations (3 mm and 6 mm for 6 mm and 12 mm plates, respectively) and 2 mm from the cut surface of specimens with dimensions of 45 × 35 × 6/12 mm. As shown in Fig. 5, both laser power and cutting mode (continuous or pulsed) significantly affect peak and cooling temperatures. The following observations are noted:

- The thermal response is primarily governed by cutting velocity and laser power. Higher velocities or lower power reduce peak temperatures due to shorter interaction times and lower energy input per unit length.
- A comparison between continuous and pulsed O_2 cutting modes indicated that the continuous mode exhibited a faster cooling rate, with overall temperatures approximately 10° C lower than those observed in pulsed mode after 10 s. This behavior is attributed to the intermittent reheating effect inherent to the pulsed operation, whereby each successive pulse prolongs the thermal exposure despite the lower instantaneous energy deposition.
- N_2-assisted cutting conditions produced notably lower peak temperatures (≤ 150 °C) than O_2-assisted ones (≥ 200 °C), primarily due to the absence of exothermic oxidation reactions. This effect is further supported by the higher gas pressures used (≥ 6 bar), which enhance convective heat transfer and facilitate more efficient removal of molten material from the kerf zone.
- Within the N_2-assisted cases, increasing the cutting velocity further ($\geq 6500\ mm/min$) reduced the peak temperatures, even under higher laser power settings. This observation underscores the dominant role of reduced heat accumulation time over the marginal increase in energy input associated with elevated power levels.

3.3 Post-LC residual stresses

Residual stress measurements were conducted on the initial four samples, i.e., SC1 through SC4, each with a thickness of 12 mm. The measurements were performed within a region located at a depth extending toward the central portion of the cut surface, as illustrated in Fig. 6.

The mid-thickness region was selected because it is significantly affected by laser-induced thermal loading while avoiding near-surface measurement artefacts associated with oxidation and surface roughness. Full through-thickness residual stress profiling was not performed due to the limited number of specimens and the high cost and time requirements of XRD measurements.

The results are shown in Fig. 7. For SC1 (6 kW, 1200mm/min), the residual stresses remained relatively uniform, stabilizing around 300–350 MPa, indicating balanced thermal gradients and limited oxidation effects. Increasing the

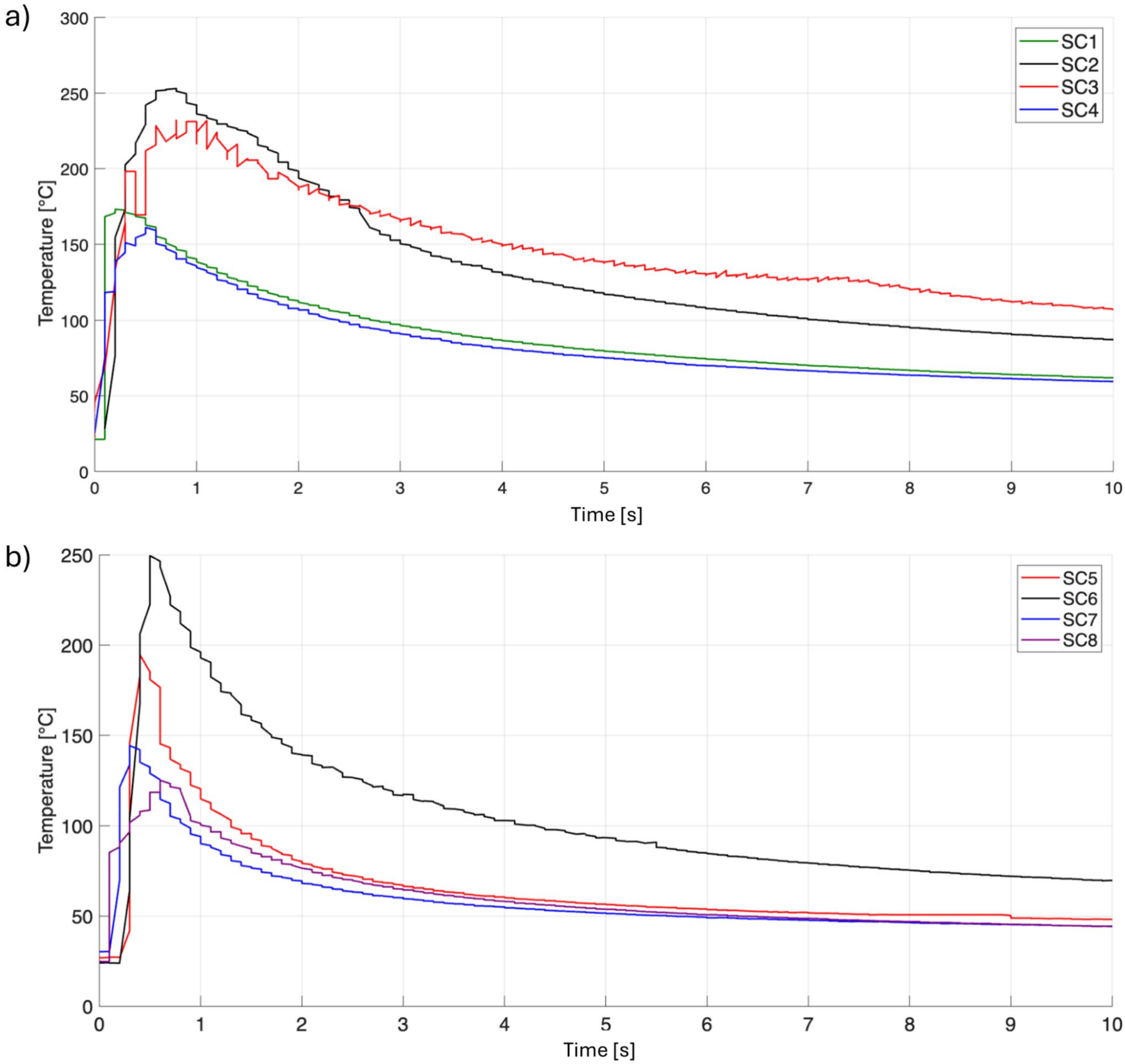

Fig. 5 Temperature-time histories relevant to Point A, observed during the (a) straight cuts for 12 mm, (b) for 6 mm

power to 12 kW and reducing the velocity to 900 mm/min in SC2 results in an overall decrease in the residual stress magnitudes, particularly for the S33 component, suggesting that a higher but steadier heat input can lead to improved stress relaxation and a more homogeneous temperature distribution. The pulsed mode of SC3 (4.5 kW, 25% duty cycle, 10 Hz, 180 mm/min) produced the steepest stress gradients. The intermittent heating–cooling cycles induced strong local thermal shocks, leading to high tensile peaks near the cut edge and significant variations across the measured distance. Conversely, SC4 (N_2, 12 kW, 4300 mm/min) showed residual stress levels comparable to those of SC1, with slightly higher values for the S22 component but similar magnitudes for S33.

The results indicate that both assist-gas type and process parameters influence residual stress formation. Although the number of investigated cases is limited, consistent trends can be identified: (i) moderate-to-high laser power ($\geq$ 12 kW) combined with reduced cutting speeds under O_2-assisted continuous-wave cutting leads to lower and more uniform residual stress distributions; (ii) pulsed cutting results in higher stress gradients due to transient thermal input and less stable melt dynamics. Based on these observations, SC2 emerges as the most balanced

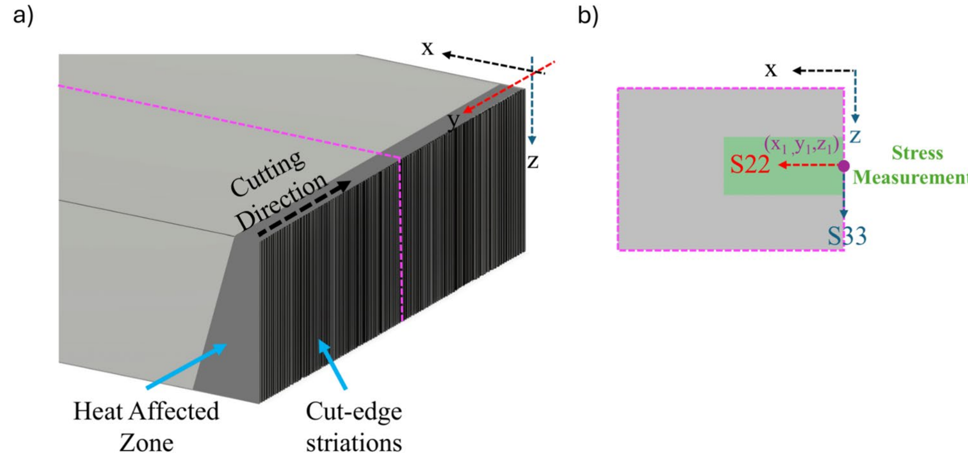

Fig. 6 Residual stress measurement configuration. (a) Laser-cut edge showing cutting direction, HAZ, and coordinate system. (b) Top view of XRD measurement area indicating S_{22} and S_{33} stress components, measured at $(x_1, y_1, z_1) = (0,\ 17.5,\ 6)\ \mathrm{mm}$

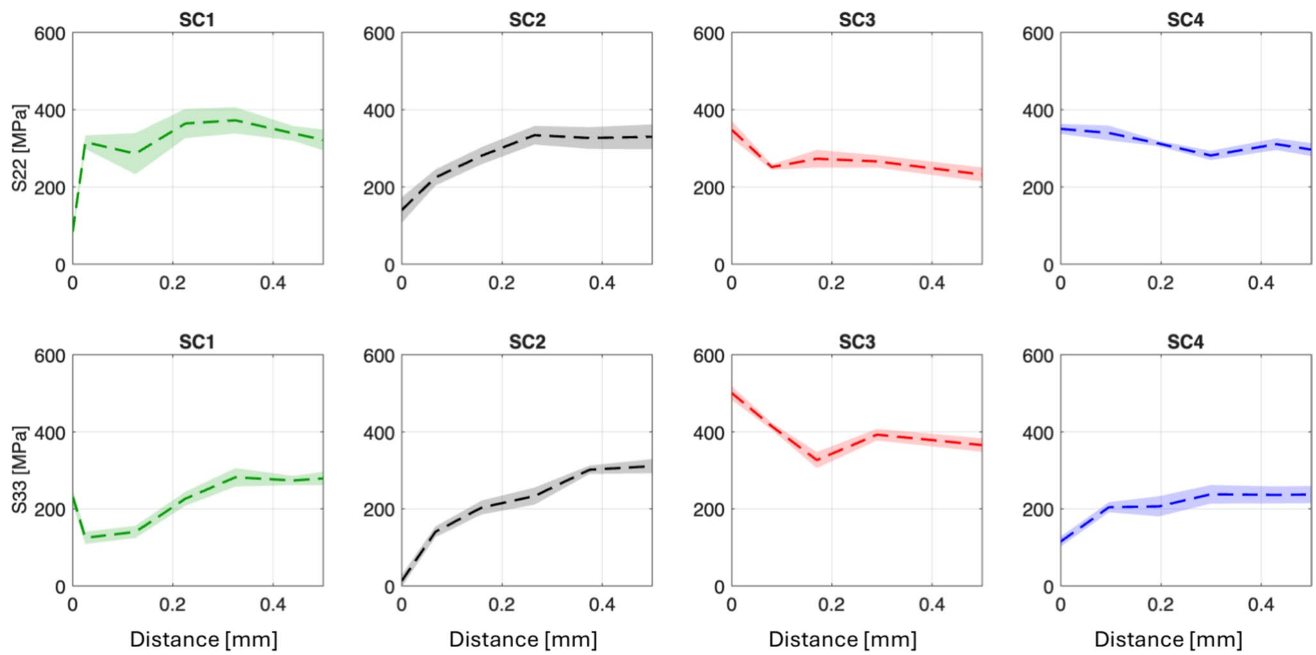

Fig. 7 Residual stresses due to various LC techniques

configuration for residual stress performance among the tested conditions.

Tensile residual stresses near cut edges can promote crack initiation and reduce fatigue life. Although fatigue performance was not directly assessed, these results highlight the importance of process parameter selection to minimize stress concentrations in structural and metastructural details. Further systematic studies are required to isolate individual parameter effects on residual stress formation. However, minimizing residual stress alone does not ensure optimal performance, as discussed in Section 4, where geometric accuracy and micro-feature fidelity after LC are shown to be equally critical for metastructural applications.

Taken together, the straight-cut experiments allow a direct comparison of how laser power, cutting speed, and assist-gas selection affect cut-surface quality and the resulting thermomechanical response. Among the tested conditions, O_2-assisted cutting performed at relatively low power and moderate speed (e.g., SC5: 4.7 kW, 3,200 mm/min, 6 mm thickness) provided the best overall balance between surface smoothness and regular striation patterns, although some localized oxidation was observed. In contrast, for thicker plates, stable and continuous cutting required O_2-assisted continuous-wave operation at higher power and lower speeds (e.g., SC1: 6 kW, 1,800 mm/min, 12 mm thickness; SC2: 12 kW, 900 mm/min, 12 mm thickness). While these conditions ensured full penetration, they also led to increased oxidation and surface roughness, particularly near the lower edge of the cut.

In contrast, N_2-assisted cutting allowed higher cutting velocities (e.g., SC7: 6 kW, 6,500 mm/min, 6 mm thickness and SC8: 12 kW, 14,000 mm/min, 6 mm thickness), resulting in reduced thermal exposure and more stable hardness profiles, while still exhibiting vertical micro-striations. Pulsed O_2 cutting conditions (e.g., SC3: 4.5 kW, 180 mm/min, 12 mm thickness and SC6: 3 kW, 400 mm/min, 6 mm thickness) showed increased surface irregularity and thermal variability due to repeated heating–cooling cycles. Overall, these indicate that straight cuts can be tailored toward specific performance objectives; surface quality (SC5), productivity and thermal moderation (SC7–SC8), or penetration capability in thick plates (SC1–SC2), and thus provide calibrated reference cases for interpreting the effects of geometric complexity.

Straight-cut experiments provide controlled reference conditions (SC1–SC8) to assess how laser power, assist-gas type, and cutting velocity influence surface quality, residual stress, and thermal response. However, real applications involve complex geometries with corners, curves, and closely spaced features, where these effects are intensified by directional changes, localized heat accumulation, and evolving melt-flow dynamics. The following section extends the analysis to such conditions, highlighting the practical manufacturing challenges encountered in real-world structural and metastructural applications.

4 Laser cutting of complex geometries

When the LC extends beyond straight paths, it introduces additional challenges, such as initial piercing, curves with varying radii, sharp corners, abrupt directional changes, and closely spaced cuts that require careful control. Building on the insights from Section 3—where straight cuts were analyzed to isolate the effects of power, speed, and gas type—the transition to complex geometries enables the evaluation of how these parameters interact under multidirectional toolpaths and localized heat accumulation. Unlike straight cuts, which primarily rely on consistent speed and power, complex shapes must accommodate rapid directional shifts, tight tolerances, and significant thermal gradients. These demands call for advanced control systems and adaptive speed modulation, which are increasingly available in modern high-end LC machines. Ensuring structural integrity and high-quality edges requires precise thermal management to avoid defects and dimensional deviations, with the kerf width, surface quality, microcracking, and dimensional consistency remaining critical. Therefore, optimizing LC parameters for complex geometries requires expertise to ensure that the resulting components meet both the quality and functional requirements. In this sense, Section 4 can be viewed as an extension of the controlled conditions studied in Section 3, straight-cut tests establish baseline correlations between LC parameters, surface quality, and thermal response, whereas the complex geometries presented here expose the limits of those correlations when directional changes and dense features amplify thermal and mechanical effects.

In light of these considerations, the primary objective of this section is to provide reference data for the performance of various fiber LC methods using different assist gas types, thereby facilitating the fabrication of intricate patterns and ensuring that the final products meet the quality objectives. To this end, a complex pattern, as shown in Fig. 8 was designed within a rectangular area measuring 20 cm × 9 cm.

LC cuts were executed using the parameters listed in Table 4, with the associated geometry-specific color codes and cutting directions illustrated in Fig. 9. In contrast to the expert-selected reference parameters employed for straight cuts in Section 3, the parameter sets examined herein correspond to geometry-dependent configurations recommended by the LC machine software for complex features. These settings were defined by the machine manufacturer based on industrial best practice and are automatically assigned to different geometric features—such as straight segments, curved paths, and small-radius details—as shown in Fig. 9. The purpose of Table 4 is therefore not to report an optimisation outcome, but to document representative, application-driven cutting configurations suitable for non-linear and dense geometries.

As highlighted in Fig. 8, the pattern fundamentally involves: (I) Corner cuts with varying angles $\theta = 4 - 90°$; (II) curves with continuous curvature change $\kappa = 0.045 - 0.7\ mm^{-1}$; (III) straight parallel cuts with decreasing spacing $0.5mm - 2.5mm$; (IV) half circles with $\varnothing = 4mm - 14mm$; (V) $\varnothing = 12mm$ polygons with $N = 8 - 18$; (VI) small square and circular holes; (VII) stars; (VIII) two types of common auxetic patterns; (IX) auxetic tetra-anti-chiral pattern; and (X) metastructural patterns with various densities. Pictures of the LC results for the three cases are shown in Fig. 10, with subsequent sections providing detailed comparative analyses using microscope images. Generally, O_2 assisted LC exhibited failure in most cuts, compared to LC assisted with N_2 and compressed air. Consequently, it is crucial to recognize that surface phenomena such as striations, oxidation, perpendicularity, and residual stress gradients tend to appear more prominently in small, curved, and closely spaced features than in straight cuts. The following subsections systematically explore these effects by geometry category (circular, corner, small holes, etc.), linking back to the baseline straight-cut behavior.

It should be noted that direct residual stress measurements could not be performed on complex geometries due to XRD limitations requiring flat and accessible surfaces. Consequently, results from straight-cut samples provide a

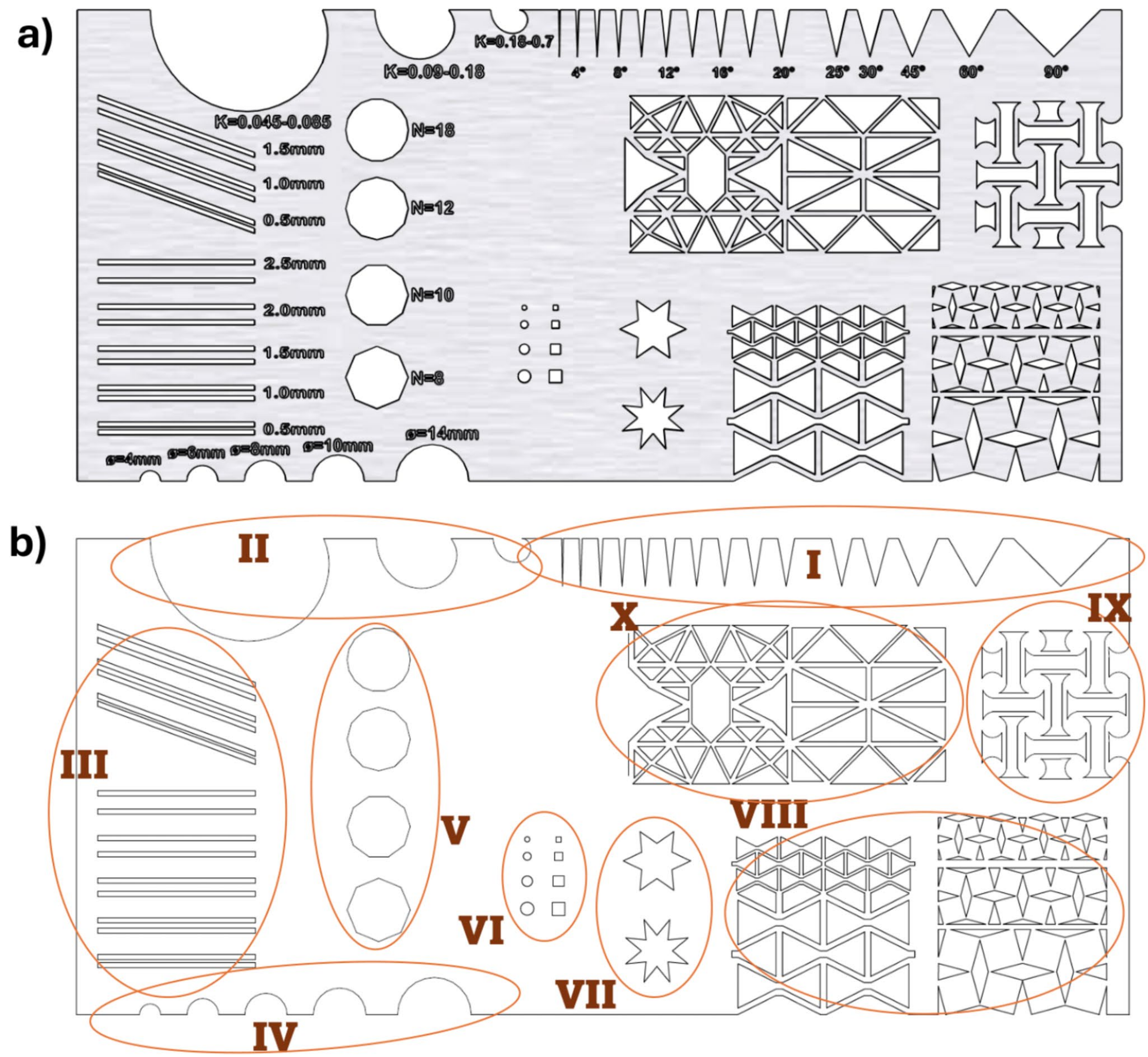

Fig. 8 Design and classification of complex LC patterns. (**a**) Experimental test panel featuring various geometrical features including angled cuts, circular holes, stars, and metastructures. (**b**) Categorization of key geometrical regions: (I) corner cuts, (II) curved paths, (III) closely spaced straight cuts, (IV) half-circular cuts, (V) polygons, (VI) small holes, (VII) stars, (VIII) auxetic patterns, (IX) auxetic tetra-antichiral pattern, and (X) metastructural patterns

Table 4 Laser Cutting Parameters for Complex Geometries. B, M, and R corresponding to blue, magenta and red lines in Fig. reffig9

#	Thick. [mm]	Power [kW]	Mode	Freq. [Hz]	Veloc. [mm/min]	Nozzle Dia. [mm]	S-off [mm]	Focus [mm]	Gas Type	Pres. [bar]
CX1-B	6	6	Cont.	–	3300	1.2	0.7	4	O_2	0.7
CX1-M	6	3.5	Cont.	–	2400	1.2	0.7	4	O_2	0.6
CX1-R	6	2.7	Cont.	–	400	1.2	0.7	3	O_2	0.7
CX2-B	6	6	Cont.	–	14000	5	0.7	-4	N_2	7.5
CX2-M	6	6	Cont.	–	8000	5	1.5	-5	N_2	10.0
CX2-R	6	6	Cont.	–	4000	5	1.5	-5	N_2	10.0
CX3-B	6	12	Cont.	–	11500	4	0.7	-3	Air	12.0
CX3-M	6	12	Cont.	–	5500	4	0.7	-3	Air	12.0
CX3-R	6	4.5	Cont.	–	1200	4	1	-3.5	Air	12.0

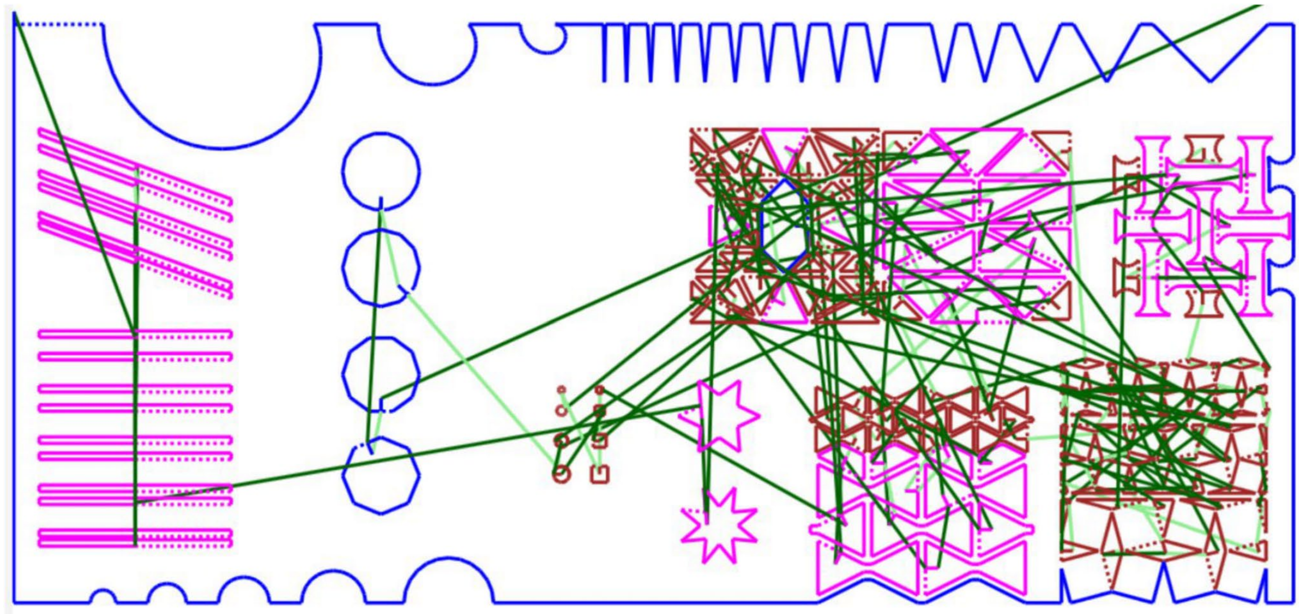

Fig. 9 Cutting path for the complex geometry (line colors depicts; (B)lue-straight/circular geometry, (M)agenta- complex geometry, (R)ed- smallest geometry, see Table 4 for cutting parameters

baseline understanding of process parameters and assist-gas effects. Although absolute stress levels in complex features may differ due to localized thermal accumulation and geometric effects, the trends observed in straight cuts are expected to remain qualitatively valid. In particular, high-power (12 kW) and low-speed (900 mm/min) O_2-assisted cutting led to reduced residual stresses. In complex geometries, only O_2-assisted cutting enables similar conditions, whereas N_2-assisted cutting requires higher speeds, making it less favorable for stress reduction. Therefore, O_2-assisted cutting is expected to yield lower residual stresses in metastructural patterns. Further validation will require advanced techniques such as micro-focus XRD, neutron diffraction, or synchrotron methods.

Complex geometric features, including corners, curved segments, intersections and narrowly spaced ligaments, impose geometry-dependent thermal and kinematic constraints, which demand coordinated adjustments in laser power, traverse speed, assist-gas pressure and focus position to preserve stability and fidelity of the cut. Accordingly, the observed effects in cut quality and dimensional accuracy arise from the coupled influence of assist-gas chemistry and the local thermal load, rather than due to gas chemistry in isolation. Normalization by energy density, while an effective descriptor for straight or isolated cuts, has limited direct transfer to densely featured metastructures, because the effective local energy input depends on the cutting direction, overlap of neighboring thermal fields and sequence of cutting passes. These limitations must be considered in interpreting the results presented in Sections 4.1–4.5.

4.1 Circular cuts

Curved trajectories inherently pose challenges in LC owing to directional changes that compromise thermal stability and disturb melt pool uniformity. As already observed in Section 3, N_2-assisted straight cuts exhibited smoother surfaces but with high variability in hardness, especially when a higher speed was utilized, whereas O_2 at reduced speeds introduced oxidation and greater perpendicularity deviations. These tendencies reappear in curved paths: N_2 provides clean edges, although circularity deviations persist, whereas O_2 maintains better geometric fidelity at the entrance side, but suffers from oxidation and deviation in the exit side owing to the higher deviation in perpendicularity. Figure 11 provides a comparative analysis of the edge quality for the smallest features from Regions II and IV.

For curved paths with continuously variable curvature (Region II), all gases produced satisfactory cuts; however, N_2 delivered the sharpest edge at the peak curvature point, O_2 showed slight oxidation, and compressed air caused increased visual roughness of the cut surface. In semi-circular cuts (Region IV), O_2 yielded the smoothest surfaces, although both N_2 and compressed air did not result in smooth circles compared to O_2. This finding is critical because circular holes are commonly employed for bolted connections, where geometric irregularities may necessitate costly post-processing. To further deepen our understanding, additional experiments with O_2 and N_2 assisted LC were conducted for full circular LC processes. For the templates considered in

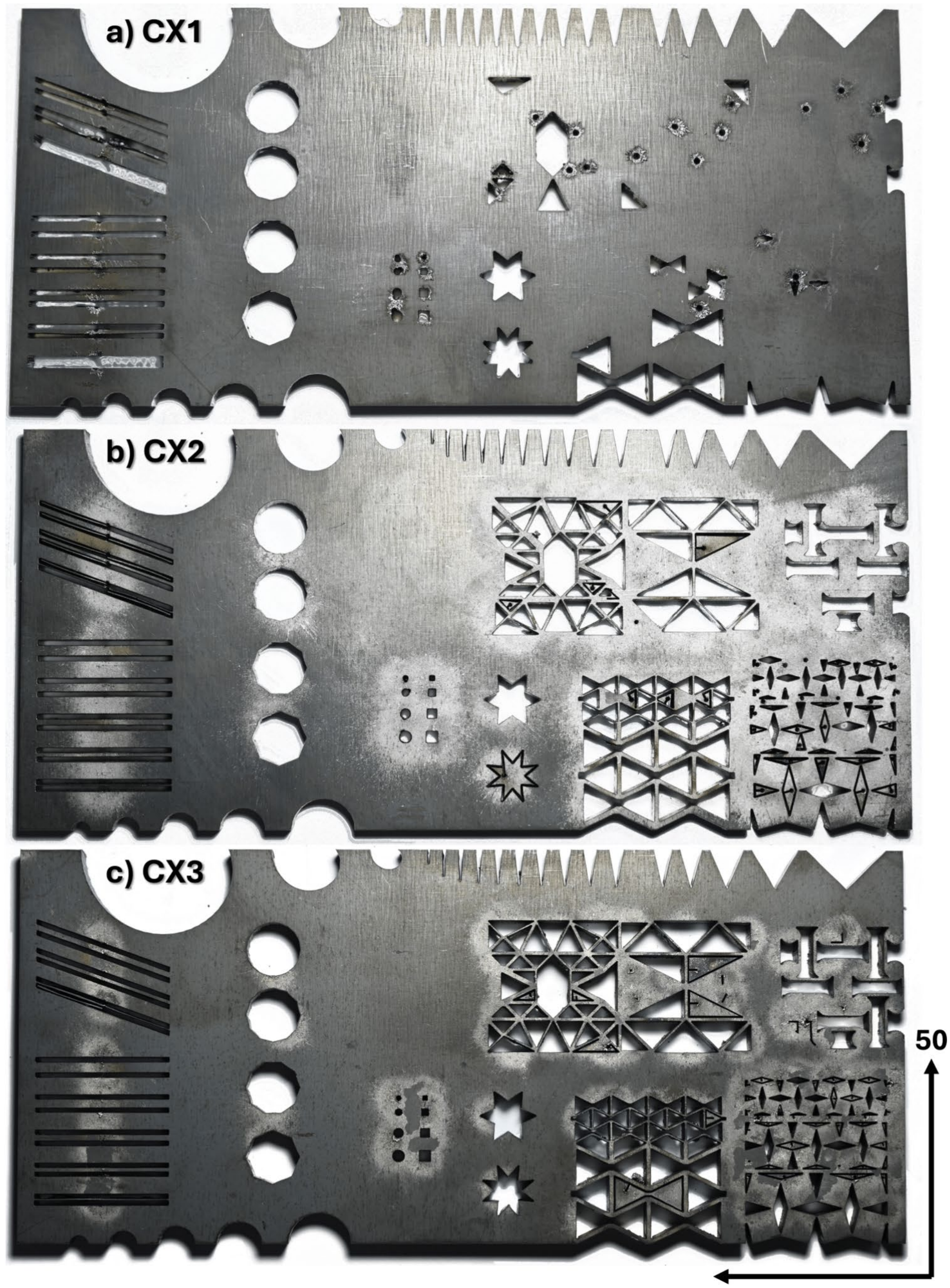

Fig. 10 Laser-cut plate images: (a) CX1, O_2-assisted; (b) CX2, N_2-assisted; and (c) CX3, compressed air-assisted (units in mm)

this study (Fig. 8), semicircles were cut from the edge and therefore did not require a piercing point.

Consequently, additional tests were performed considering square elements with dimensions of 35 × 35 mm and a thickness of 12 mm, and holes with a diameter of 12 mm were cut using LC, as shown in Fig. 12. Four different LC techniques (CC1-CC4), detailed in Table 2, were visually compared. Visual inspection of the circular cuts revealed a consistent surface quality with similar color owing to oxidations and characteristics of straight cuts, as expected from the precise control of the laser beam employed during curved motions. A significant difference was noted in the initiation point of the LC process, specifically in the piercing location. To obtain a smoother circle, each circular cut begins with a piercing in the center of the circle, followed by the path illustrated in Fig. 12. Point D, known as the lead-in point, is particularly significant because it marks the shift from horizontal to circular motion, necessitating focused attention. Microscopic inspections are presented in Fig. 13 highlights the key surface characteristics on both the damaged (D) and damage-free (DF) sides after lead-in/lead-out cutting for different LC techniques:

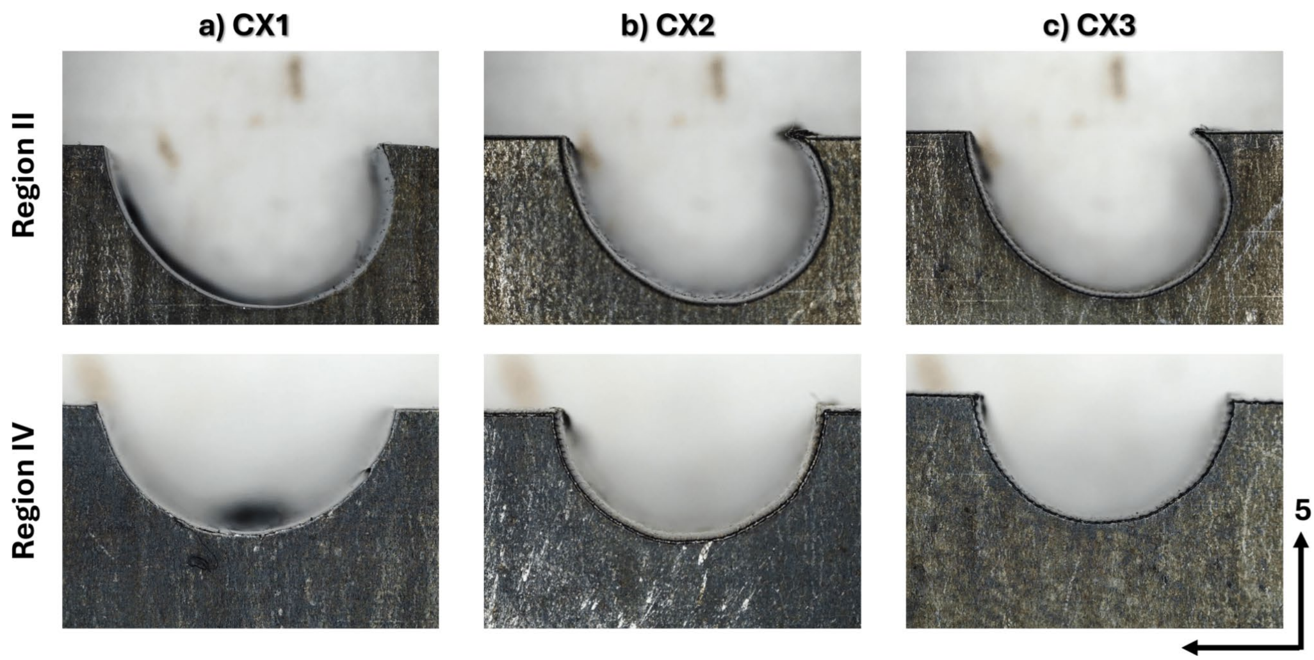

Fig. 11 Microscope 80x magnified views of circular cuts showing the smallest features: Region II with curvatures $\kappa = 0.18\text{–}0.7\ mm^{-1}$, and Region IV with a circular cut of diameter $\varnothing = 4\ mm$ (units in mm)

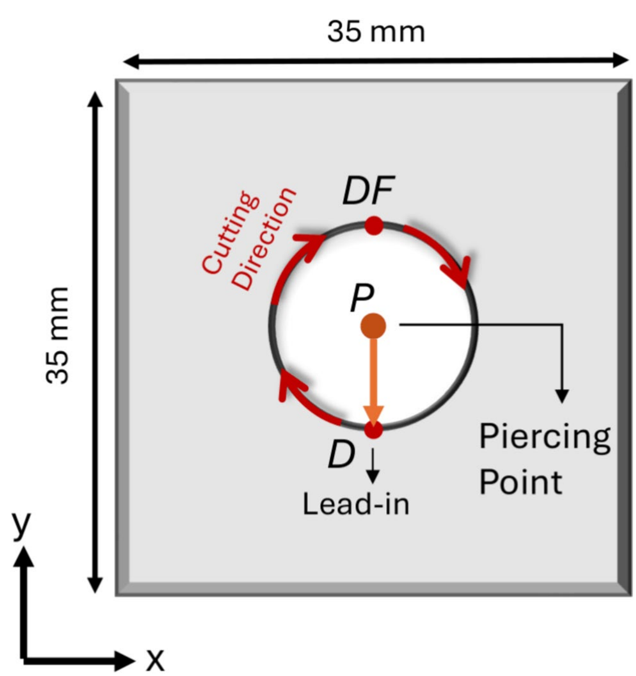

Fig. 12 Geometry and setup for circular LC. The cutting path starts at the piercing point (P) and follows a counterclockwise direction, forming damaged (D) and damage-free (DF) zones

- CC1 reveals thermal damage and irregular striation patterns. The D side exhibited considerable melt re-solidification and striation disruption, suggesting inadequate energy control near the lead-in path. The DF side, while smoother, still contained visible micro-spatter and evidence of thermal degradation.
- CC2 shows striations-free surface and lower surface disruption. Minor signs of local melting and spatter are present, but the overall thermal impact is less severe than in CC1, indicating more effective process control.
- CC3 displays high oxidation and non-uniform groove formation. Side D exhibits discoloration and uneven melt buildup with disrupted striation patterns. In contrast, the DF side maintains better alignment, although it displays variations in groove depth and residual heat effects, indicating a partial compromise in surface integrity.
- CC4 exhibits severe thermal degradation and surface contamination. The D side shows extensive resolidified melt zones, high roughness, and overheating. The DF side is also notably rough, with indistinct striations and widespread thermal imprints, suggesting excessive energy input during the lead-in/lead-out stages.

Across all cutting conditions, the D sides consistently experienced a higher thermal impact, and the recurring presence of molten deposits, oxidation, and disrupted striations on the D sides underscores the importance of optimizing lead-in/out strategies to minimize heat concentration and improve edge quality.

4.2 Corner cuts

In Fig. 14, comprehensive details are given regarding the LC of sharp corners with varying angles. The straight-cut

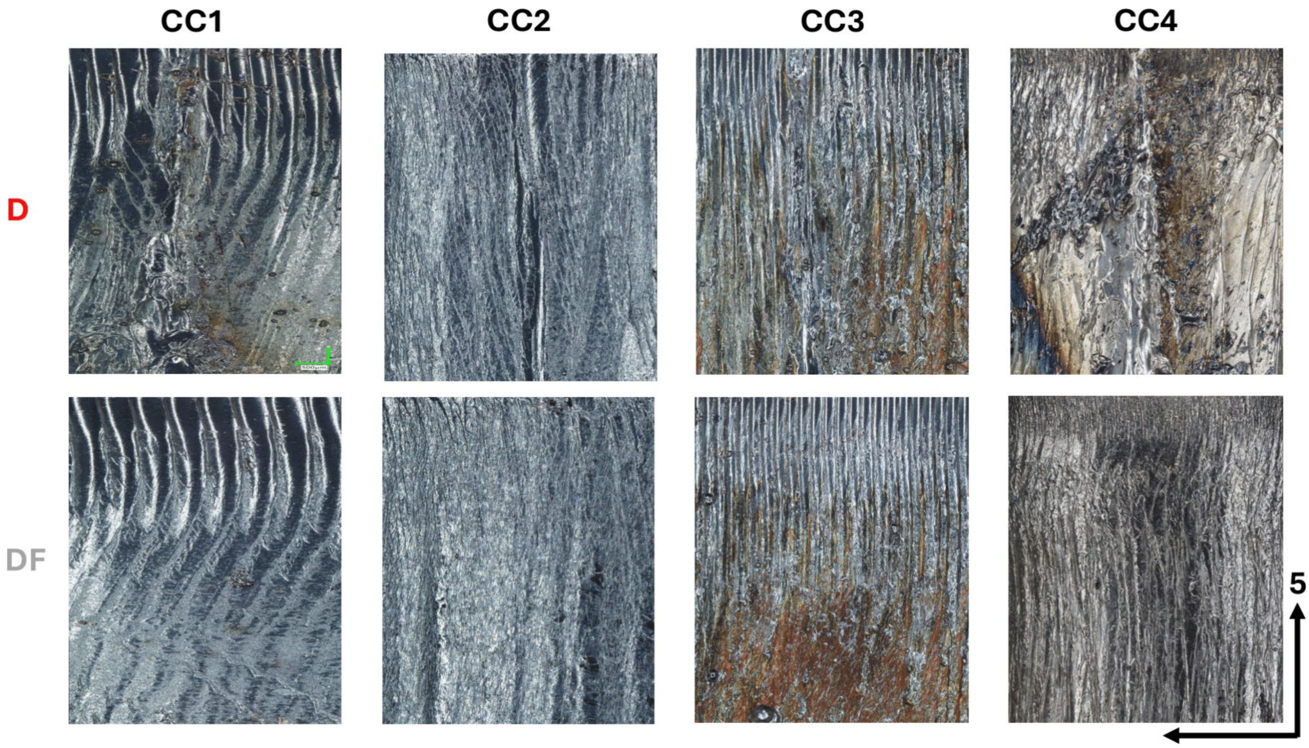

Fig. 13 Microscopic pictures for lead-in out damage on the surface for the LC techniques from CC1 to CC4 for 12 mm diameter of holes (D: Damaged side, DF: Damage-free side, and units in mm)

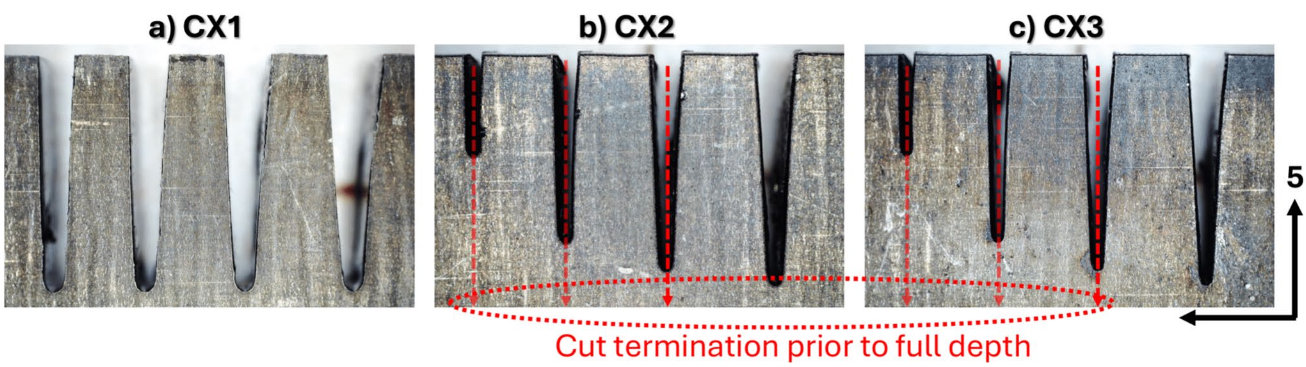

Fig. 14 Details of sharp corner LC from Region I (from left to right corner angles corresponds to 2°, 4°, 6°, and 8°, and units in mm).

analysis demonstrated that a higher thermal input in the O_2 mode reduced the hardness and promoted perpendicularity. At the corners, these effects become more pronounced owing to the accumulation of heat in the deceleration zones, which accounts for O_2's excessive melting and poor definition of the kerf. On the other hand, the diminished thermal impact of N_2, which maintains hardness in straight cuts despite variations in roughness (SC7–SC8), allows for a more precise kerf definition at sharp angles. O_2 demonstrated the capability of cutting the smallest corner angle assessed (i.e., 2°) thanks to the smaller beam diameter; however, the required detail level could not be achieved. In the other two scenarios, LC was unable to cut corners smaller than 6°; the minimum feasible corner angle identified for N_2 and compressed air was 8°. In terms of dross and burrs, N_2 exhibited the best results, while O_2 led to excessive melting and poor kerf definition, especially in deceleration zones, while compressed air performed moderately.

4.3 Small holes

In Fig. 15, the LC results for Region VI are presented also with images from the bottom surfaces. The straight-cut results showed that O_2 at lower power/medium speed (SC1) achieved smooth surfaces but suffered from significant perpendicularity deviations, whereas N_2 introduced

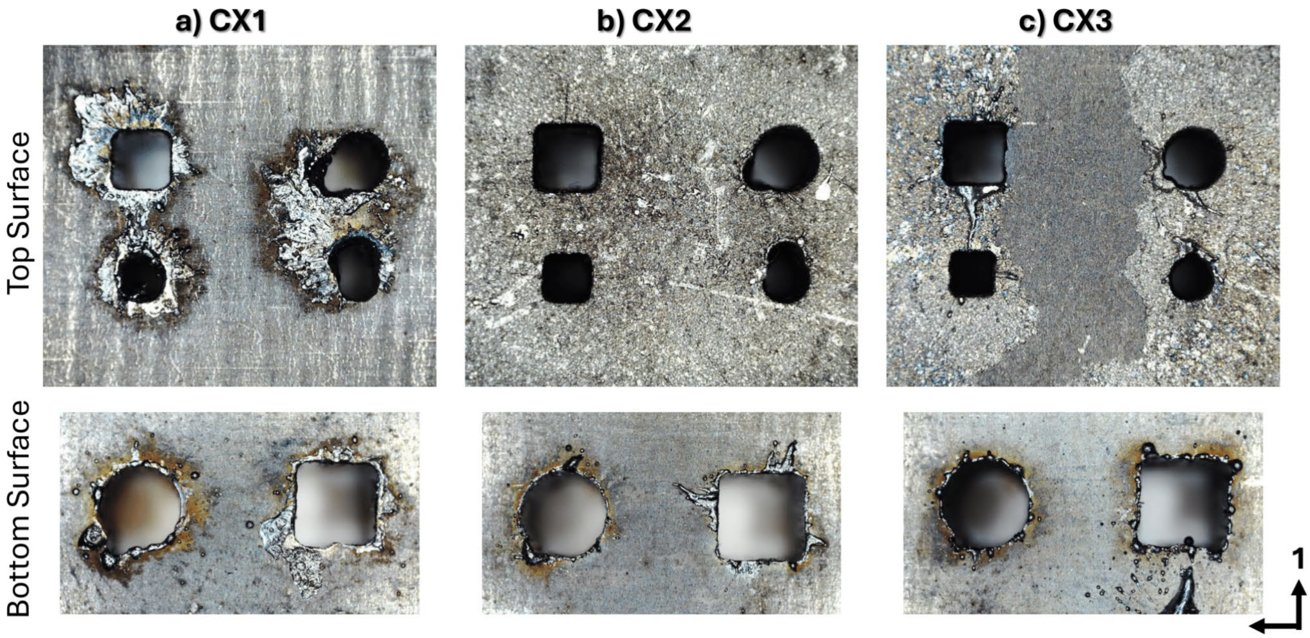

Fig. 15 Detailed views of LC performance in small-hole features, highlighting differences in hole definition, edge integrity, and defect formation under different assist-gas conditions (units in mm)

variability in hardness. The same constraints are evident in small holes: O_2 is unable to create accurate shapes owing to size inaccuracies and a lack of perpendicularity, whereas N_2 has difficulty with circular holes. In contrast, compressed air provides better accuracy, although it results in dross buildup. In the case of small holes, where precision is critical, perpendicularity deviations result in irregular geometries. This behavior limits the applicability of O_2-assisted cutting. Similarly, for circular holes, O_2 failed to achieve precise circles, even for larger diameters.

N_2 cannot create a circle for the smaller hole. Consequently, compressed air demonstrated superior hole cutting performance in terms of accuracy. However, an inspection of the bottom of the plate, specifically the exit side, showed that compressed air caused a considerable amount of dross to form around the holes, which required additional processing.

4.4 Closely spaced straight LC paths

Closely spaced LC paths lead to thermal accumulation and feature interaction. This effect is particularly pronounced in dense geometries such as slits, notches, and hole clusters. Section 3 showed that the increased thickness and medium speed increased the surface roughness and oxidation (SC2). In closely spaced cuts, the same mechanisms observed in straight paths are amplified. O_2 produces excessive heat, melting, and oxidation between adjacent kerfs, whereas N_2 partially mitigates thermal effects but remains sensitive at piercing points. Compressed air balances the thermal input and dimensional fidelity but requires post-processing owing to dross. Figure 16 compares the performances in Region III.

In the top row of Fig. 16, where the cuts are restricted to the horizontal axis, the application of O_2 results in substantial thermal distortion in the steel, excessive melting, and oxidation between the adjoining cuts. N_2 achieved the most optimal outcomes, characterized by minimal thermal influence and well-defined kerf edges. The use of compressed air produced results of moderate quality with discernible roughness and moderate discoloration. Conversely, O_2 exhibited the poorest performance, failing to adequately separate two closely aligned rows of horizontal cuts.

In the middle and bottom rows of Fig. 16, parallel cuts were performed at an angle. This required the LC machine to control the X- and Y-axes simultaneously. This resulted in more problems in cutting, as can be seen in the given images, and better highlighted the difference between compressed air and N_2. O_2 again led to deformation and burrs at notch tips and was not able to cut parallel lines even when the spacing was increased (bottom row). N_2 was able to maintain the middle thin piece, yet its piercing point damaged it and divided it into half. This was also observed even when the spacing was increased. On the other hand, compressed air showed the best results, being able to cut two parallel angled lines and keep the middle piece intact. Overall, compressed air demonstrates cutting fidelity and is most suitable for densely packed features, although it necessitates

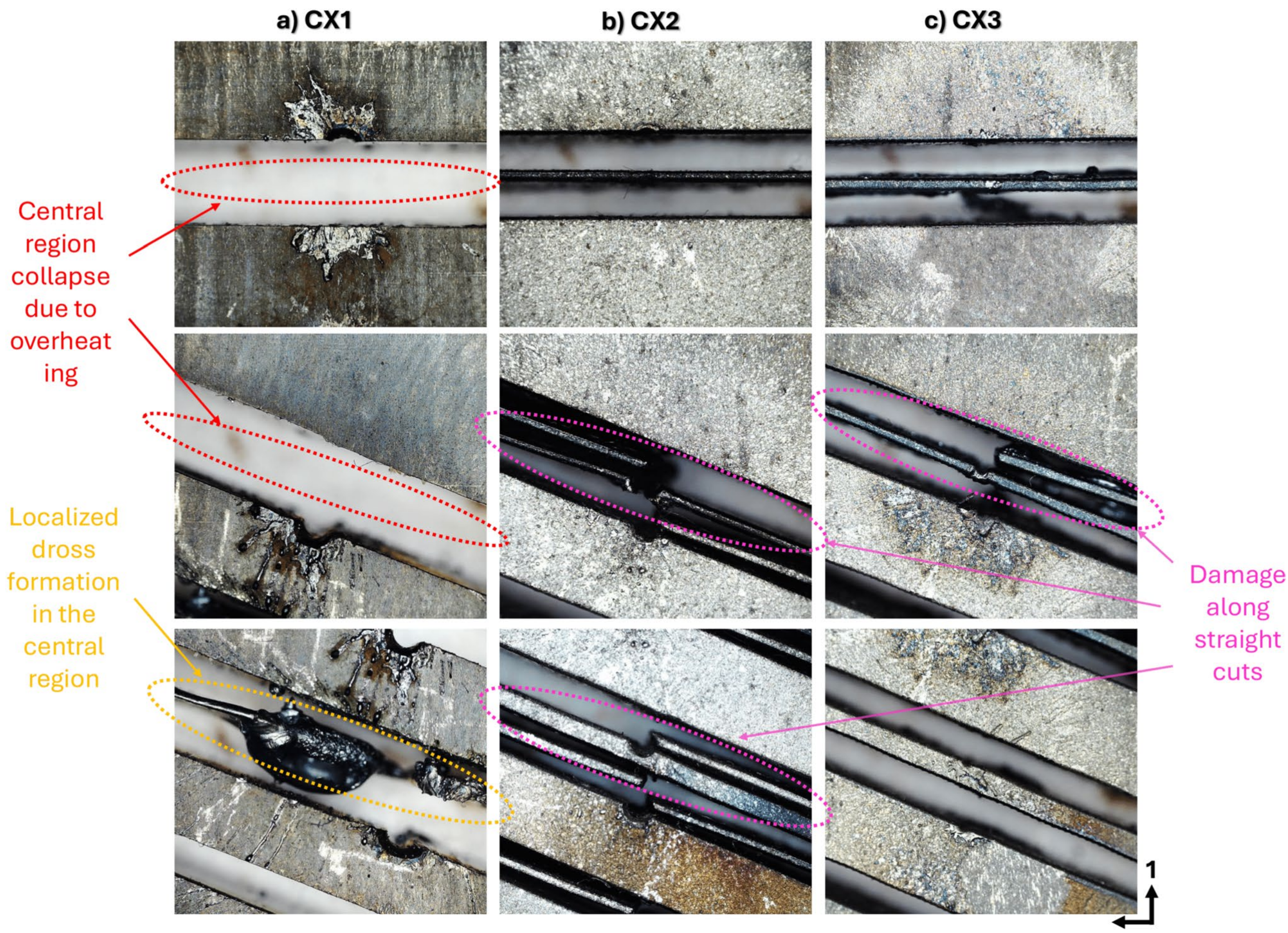

Fig. 16 LC performance in closely spaced features. Top row horizontal cuts with 0.5 mm spacing, middle row angled cut (20°) with 0.5 mm; and bottom row with 1 mm spacing (units in mm)

post-processing. O_2 introduces significant thermal degradation, and N_2 is of moderate quality. Section 3 demonstrated that increased thickness and slower speed in straight cuts increased the surface roughness and oxidation with thermal accumulation. The same mechanisms govern closely spaced paths: heat buildup between adjacent cuts, especially under O_2, whereas N_2 mitigates some effects but still shows sensitivity at piercing points, also highlighting the importance of the beam diameter.

4.5 Dense and intricate patterns

Fine-feature cuts, such as stars, auxetic geometries, and metastructural patterns, are highly sensitive to heat input. They are also strongly influenced by path complexity. The variation in the perpendicularity of O_2 and N_2 straight cuts at varying speeds results in dimensional changes and thicker elements in intricate designs, thereby reducing precision. Figure 17 shows the star-shaped cuts (region VII) produced using O_2, N_2, and compressed air assistance. Although all three gases successfully completed the cuts, the resulting edge qualities differed considerably. Compressed air-assisted cutting yielded the most accurate profiles, characterized by sharp edges and minimal burr formation. N_2-assisted cutting exhibited slight edge roughness and surface discoloration, whereas O_2-assisted cutting led to pronounced oxidation, particularly evident at the tip of the stars. Nevertheless, eight pointed stars of N_2 were stuck in place owing to the micro-joint formation at the bottom surface.

Figure 18 shows auxetic patterns (region VIII), where only N_2 and compressed air succeeded, as shown in Fig. 10. O_2 failed to complete the cuts owing to overheating that was pre-identified through the LS7 controller software and skipped during the LC process. Compressed air delivered a better edge definition and completed the pattern even with the smallest features. N_2 cutting introduced deformation and color change, especially in thin sections. Moreover, of the greatest importance, N_2 failed to cut several small features. Most importantly, N_2 results in a second pattern that does not match the supplied CAD design.

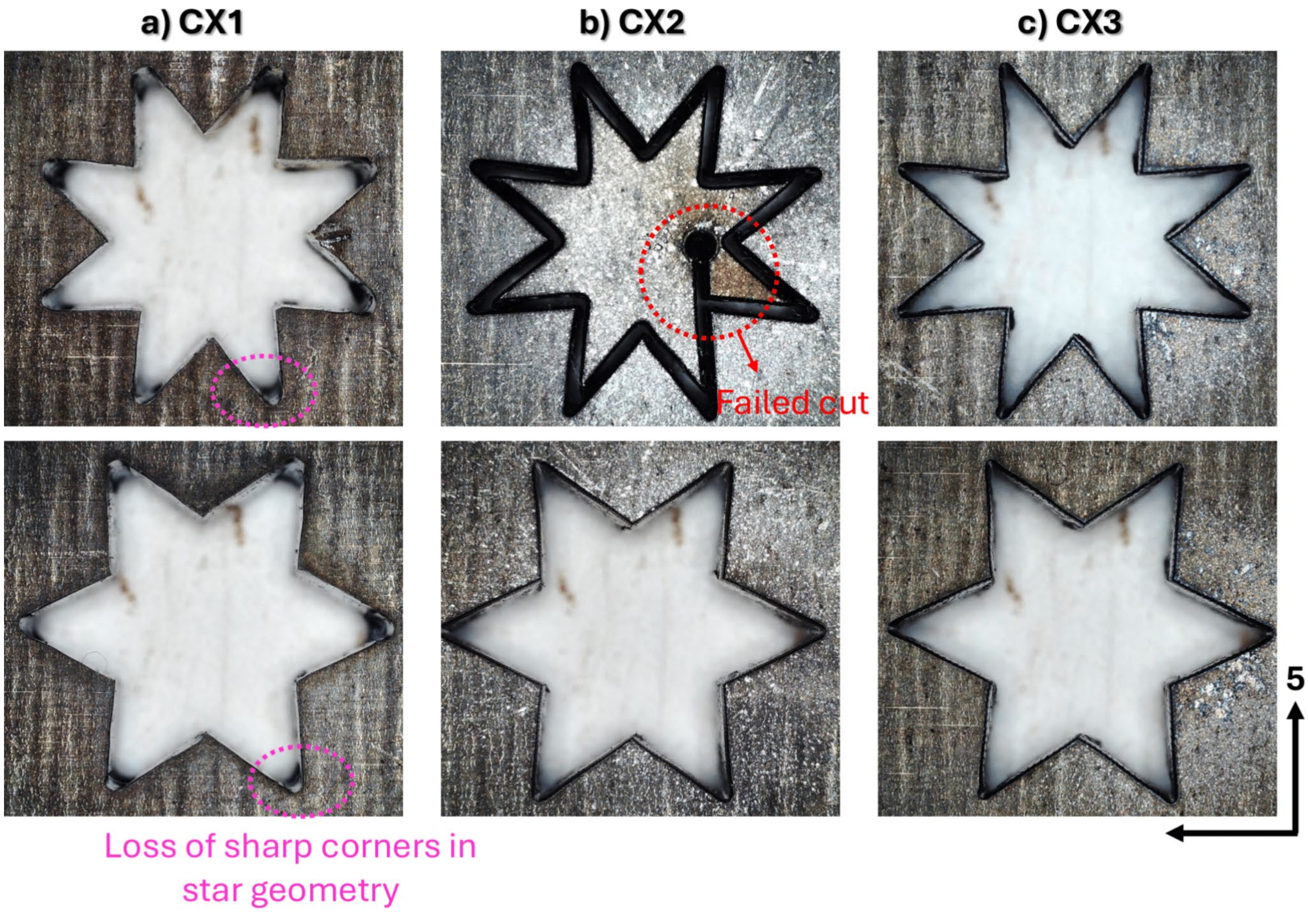

Fig. 17 Comparison of star-shaped laser-cut features (Region VII), highlighting differences in feature definition, corner integrity, and defect formation under different assist-gas conditions (units in mm)

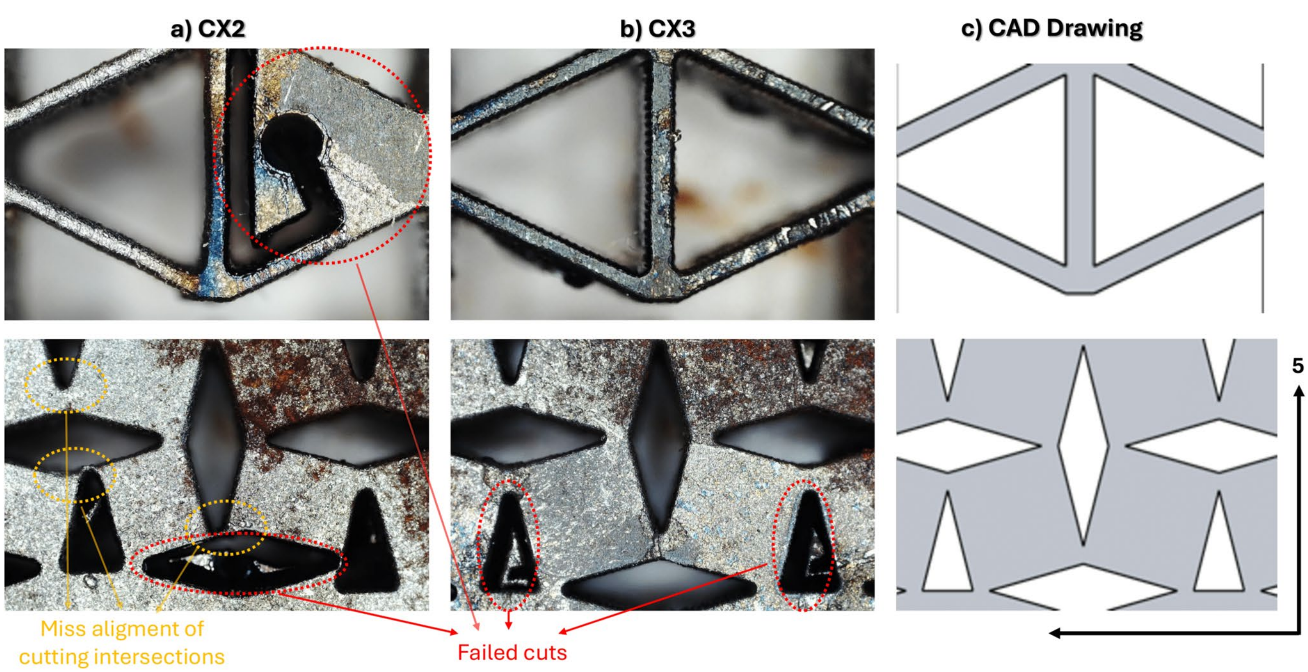

Fig. 18 Fine-feature laser cuts in region VIII using (**a**) N_2, (**b**) compressed Air, and (**c**) CAD drawing (units in mm)

Finally, focusing on auxetic tetra-anti-chiral and meta-structural patterns, a major drawback of N_2 was identified. As shown in Fig. 19, and in contrast to compressed air, N_2-assisted LC resulted in significant deviations from the nominal design geometry provided to the LC machine. Overall, even though compressed air-assisted LC requires post-processing due to increased roughness and the gross collected in the bottom surface, it proved to be more effective for cuts demanding dimensional accuracy and, more generally, for producing smaller features and sharper angles. The observations from N_2 in auxetic patterns are consistent with the findings in Section 3, where N_2-assisted straight cuts displayed high variability in hardness despite the favorable surface roughness. This suggests that under highly intricate geometries, the same variability translates into dimensional drift and feature thickening. Compressed air, while rougher and requiring post-processing, better preserves the geometric fidelity.

Building on the residual stress and thermal trends observed in straight cuts, a conceptual understanding of thin-ligament behavior in dense and/or intricate patterns can be outlined. Thermal accumulation in tightly spaced cuts or small-featured metastructures leads to localized stress concentrations, particularly in thin sections. O_2 produces due to low velocity, result in excessive heat, which increases melting and oxidation; despite higher heat input reduces the residual stresses. In N_2 side, it reduces thermal exposure but may still generate tensile stresses at piercing points due to the high velocity. These stress–thermal interactions explain the observed failures or deformations in thin ligaments, such as feature thickening, micro-joint formation, or deviation from nominal geometry, and provide a rationale for the differential performance of assist gases in complex patterns.

Overall, the results indicate that corner cuts can be successfully achieved using oxygen-assisted cutting (O_2, CX1) down to sharp turns of approximately 1 mm. Moreover, all investigated cutting technologies are capable of producing circular holes with diameters as small as 2 mm, as well as square features with dimensions of 2 mm × 2 mm. For closely spaced geometries, the best performance is observed for 1 mm inclined, double-sided cuts with a 20° inclination angle when using compressed Air (CX3). In addition, compressed Air cutting (CX3) enables the successful fabrication of well-defined star-shaped patterns with a side-to-side length of 10 mm, as well as very small rectangular features with side lengths of approximately 3 mm. In terms of cutting reliability, the observed failure rates are approximately 70 %, 40 %, and 25 % for O_2 (CX1), N_2 (CX2), and compressed Air (CX3), respectively.

5 Conclusion

This work presents an experimental study of fiber LC of S235 structural steel across two classes of geometrical complexity—straight cuts and architected, densely featured patterns—with oxygen, nitrogen, and compressed air as assist gases. The impact of LC parameters, with a main focus on assist-gas type, on cut quality, thermal behavior, residual stress formation, structural integrity, dimensional deviations from nominal design, surface quality, and post-processing

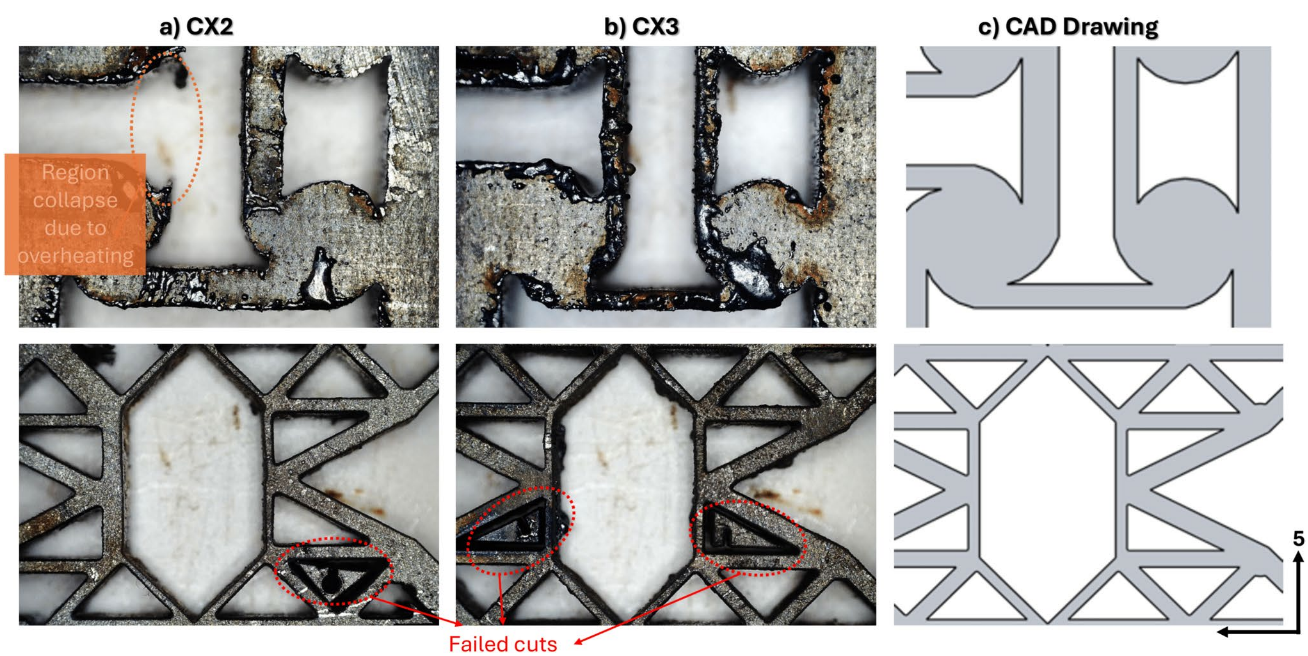

Fig. 19 Fine-feature laser cuts in region IX and X using (**a**) N_2, (**b**) compressed Air, and (**c**) CAD drawing (units in mm)

requirements were investigated. This study integrates high-resolution digital microscopy, roughness/perpendicularity/hardness metrology, infrared (IR) thermography with emissivity calibration, and X-ray diffraction (XRD) residual stress measurements. The main conclusions are as follows:

- For 6 mm plates, low-velocity N_2 (SC7) yielded the lowest roughness ($R_{z5} \approx 10\,\mu$m) and reduced surface hardening, while for 12 mm plates, moderate-speed O_2 (SC2) produced the best overall balance of roughness ($R_{z5} \approx 20\,\mu$m), and perpendicularity. Across thicknesses, increases in the heat input (via power and reduced speed) amplified the roughness variability, which is in agreement with the IR thermal fields.
- XRD results confirmed tensile residual stress patterns near cut-edge, with moderate-speed O_2 (SC2) cutting exhibiting the most favourable and uniform distribution, pulsed O_2 (SC3) showing the steepest gradients, and high-speed O_2 (SC1)–N_2 (SC4) cases yielding comparable intermediate values.
- In curves, tight corners, closely spaced passes, star/polygon features, and auxetic/chiral metastructural patterns, compressed air provided the highest geometric fidelity and feature survivability, particularly where thermal bridging and local heat accumulation are critical. However, this resulted in a higher dross on the exit side, that is, the bottom surface, as shown in Fig. 20, requiring post-processing. O_2 frequently failed in dense patterns owing to overheating and melt coalescence, whereas N_2 completed many shapes but produced thicker-than-nominal ligaments and discoloration on thin features. For closely spaced, angled parallel cuts, compressed air uniquely preserved the intermediate web, N_2 often damaged it at the piercing/lead-in, and O_2 failed completely.
- Circular and curved cuts highlighted a trade-off between geometric accuracy and surface condition: O_2 improved circularity and edge smoothness but at the cost of oxidation; compressed air and N_2 resulted in higher dross on the exit side. Lead-in/out control dominated the local defects around the piercing point, suggesting that optimized entry strategies are as influential as the bulk parameter sets for hole quality.
- The results highlighted the influence of assist-gas selection on the manufacturability of fine-featured metastructural patterns. The required geometric fidelity achieved with compressed air-assisted LC demonstrates its suitability for producing small-scale features and sharp auxetic geometries essential in metastructure fabrication, where precision governs mechanical performance. Conversely, the deformation and dimensional drift observed with N_2 underscore the limitations of relying solely on surface-finish metrics, emphasizing that accurate feature reproduction is critical for ensuring the intended mechanical response and functional integrity of metastructures
- The findings reveal that not all metastructural or auxetic geometries are readily manufacturable by LC, as laser–material interactions impose intrinsic constraints on achievable feature resolution and dimensional accuracy. This underscores the necessity of integrating manufacturability considerations, such as heat input and minimum feature size, early in the design and optimization

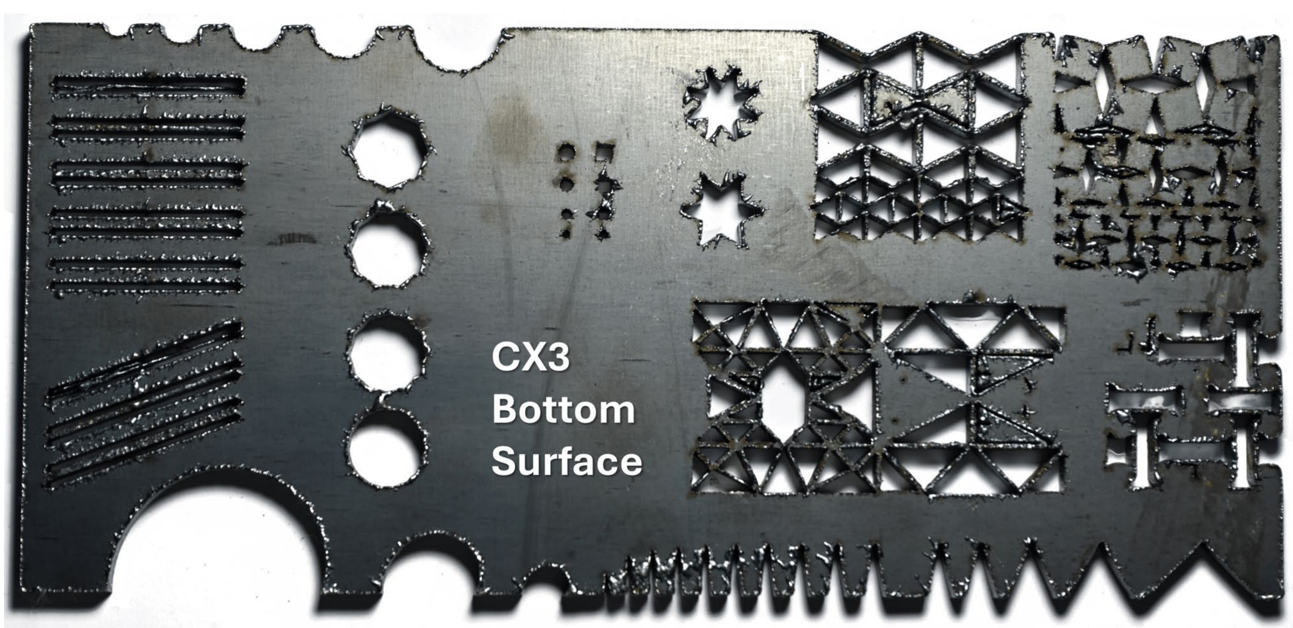

Fig. 20 Bottom surface of CX3 (compressed air-assisted LC) sample

stages of metastructure research. Embedding these practical constraints from the outset is essential to ensure that theoretically optimized architectures can be physically realized without compromising their intended functionality or performance.

The actionable guidance for LC of structural and metastructural parts obtained from the given study can be summarized as follows:

- For straight cuts, choose high-velocity N_2 (SC8) for 6 mm when roughness and low surface hardening are paramount; choose moderate-speed O_2 (SC1) for 12 mm when roughness/perpendicularity must meet tighter tolerances with limited cycle time. Use high-power and moderate speed (SC2) O_2 where residual-stress management is critical, and then verify the local stress heterogeneity.
- For complex and dense patterns prefer compressed air-assisted LC to maximize fidelity of sharp corners, thin webs, and tightly spaced features; budget for mechanical/abrasive post-processing to remove exit-side dross. Avoid O_2 in thermally congested regions; use N_2 only where slightly thicker effective kerfs are acceptable.
- For holes and bolting employ O_2 with carefully tuned lead-in/out for superior circularity; if using N_2/compressed air, anticipate additional reaming/deburring on the exit face.

In terms of limitations, despite emissivity calibration, IR thermography remains line-of-sight and surface-weighted; subsurface gradients and through-thickness phase changes were inferred rather than measured directly.

Future work should: (i) investigate adaptive lead-in/out strategies and path-speed modulation to suppress defects near piercing points and deceleration zones; (ii) extend experimental validation to curved surfaces and circular holes under mechanical stress tests, quantifying the combined influence of surface roughness, HAZ hardness, and residual stresses on endurance; (iii) embed a multi-objective optimization framework to produce process maps that balance roughness, perpendicularity, HAZ characteristics, residual stress states, and productivity- or efficiency-based metrics, enabling a combined assessment of structural performance and process efficiency for both conventional structural details and high-resolution metastructures; and (iv) conduct systematic testing of LC-fabricated metastructural patterns, benchmarking their mechanical performance against numerical predictions, with further attention to long-term fatigue behavior. Moreover, a detailed metallographic examination of cut edges and heat-affected zones is identified as an important topic for future work.

Appendix Calibration of thermal camera and emissivity

To verify that the IR camera can accurately capture the temperature near the laser beam, a comparison with a thermocouple, as shown in Fig. 21, was conducted. It was verified that the IR camera could capture the temperature within a margin of error that could be calibrated. The difference between the thermal camera and thermocouple was connected to: i) the thermocouple acquisition frequency was limited (1 Hz) and was not able to capture the rapid temperature change, and ii) the attachment method of the thermocouple restricted heat conduction. These findings indicate that the thermal camera exhibits a higher precision.

The infrared camera measures the radiative energy emitted by a surface and converts it into surface temperature using

$$T_{\text{surf}} = \left[\frac{E}{\sigma\epsilon_{\text{surf}}}\right]^{1/4} \quad (1)$$

where T_{surf} represents the surface temperature in Kelvin (K) and E denotes the radiative energy emitted from the surface per unit area in watts per square meter (W/m²). Herein,

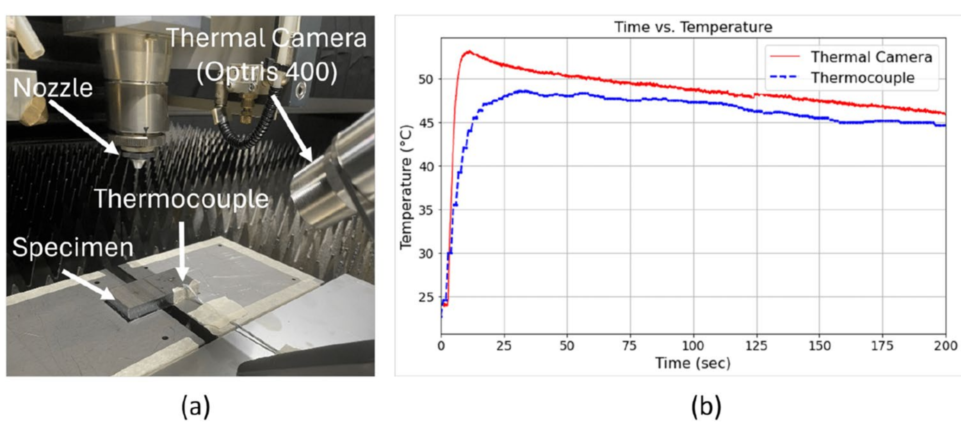

Fig. 21 Temperature distribution comparison between thermal camera and thermocouples: (**a**) experimental setup, (**b**) temperature time history of LC process

ϵ_{surf} is the dimensionless surface emissivity coefficient that can take a value between 0 and 1, indicating the efficiency with which the surface radiates compared to a perfect black body. σ, the Stefan-Boltzmann constant, has a value of $5.670 \times 10^{-8}\ \mathrm{W\ m^{-2}K^{-4}}$, relating the radiative energy to the fourth power of the surface temperature. This equation is crucial for determining the surface temperatures from the radiated energy in thermal analysis using infrared cameras.

To calculate emissivity, half of the sample was coated with a low-reflection black paint of known emissivity ($\tilde{1}$), and temperature data obtained from the coated and uncoated sides were compared. The details of the sample and measurement are shown in Fig. 22. Accordingly, the temperature data were evaluated with emissivity coefficients in the range of 0.5 to 1, and the results are given in Fig. 23 It was observed that the increase in the temperature resulted

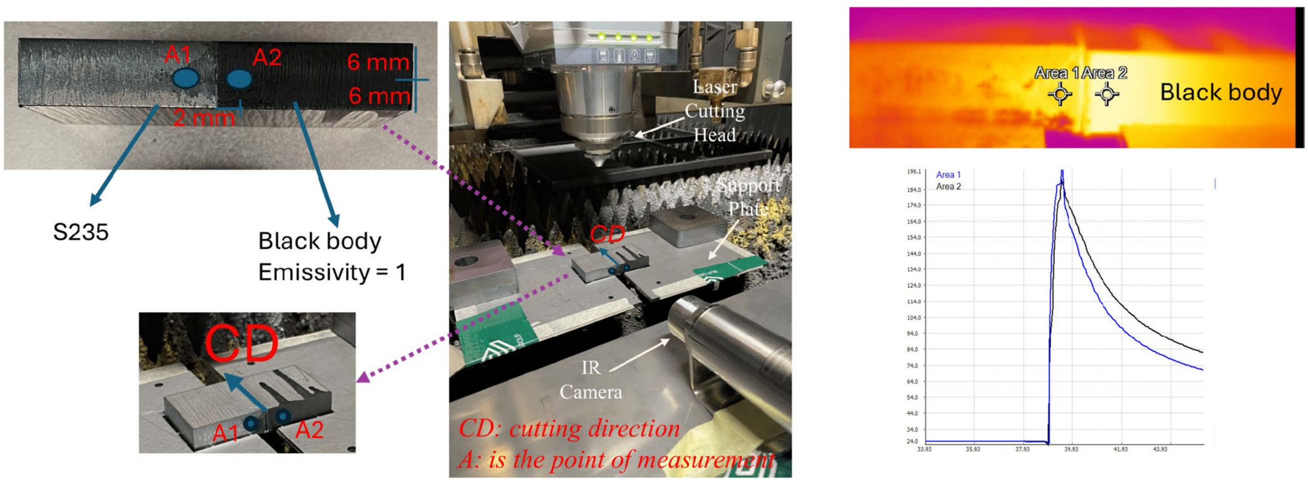

Fig. 22 Emissivity measurement for S235

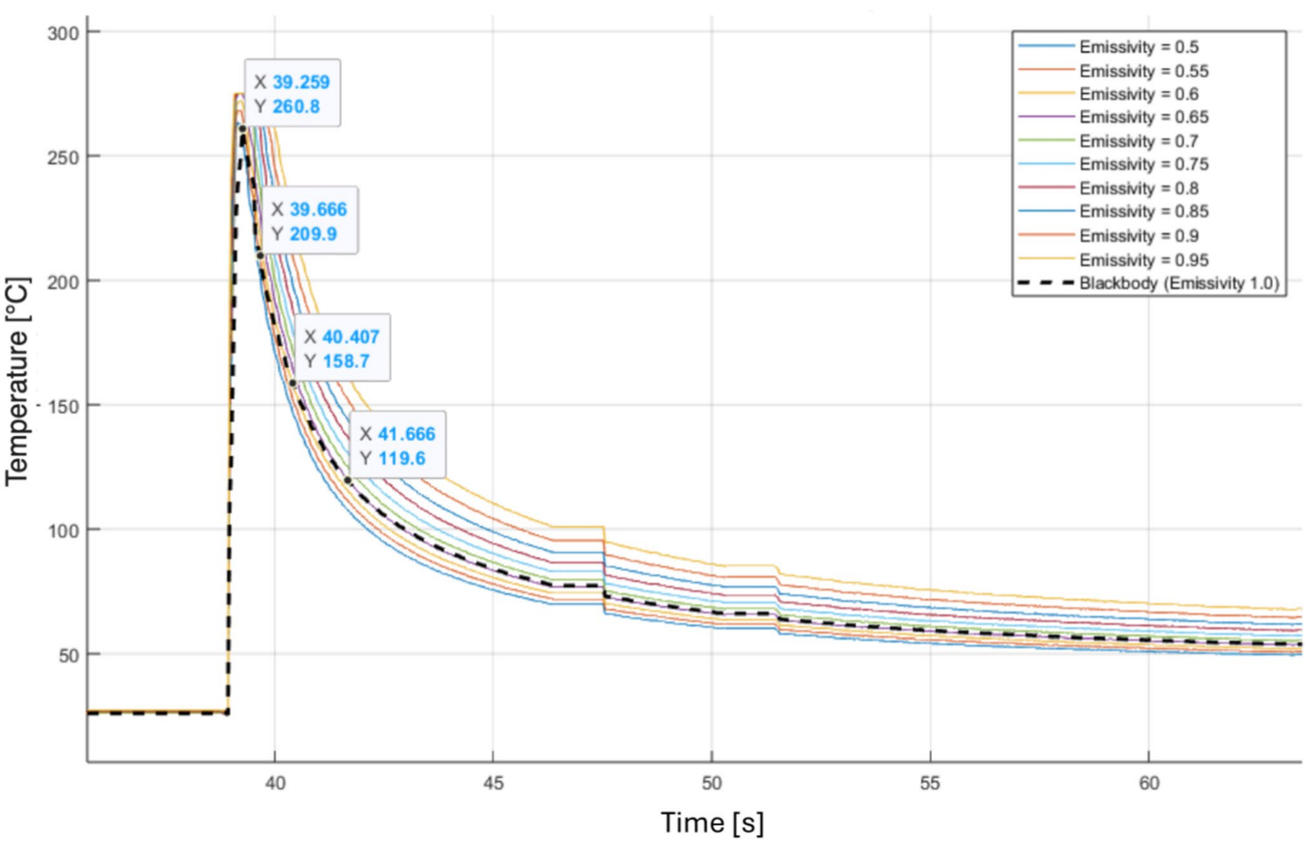

Fig. 23 Emissivity values for temperature-time history for S235

in a decrease in emissivity value. Consequently, the calibrated emissivity values at different temperature ranges are reported as

$$\epsilon_{\mathrm{surf}} = \begin{cases} 0.5 & \text{if } 250°C > T > 210°C \\ 0.55 & \text{if } 210°C > T > 160°C \\ 0.6 & \text{if } 160°C > T > 120°C \\ 0.65 & \text{if } 120°C > T. \end{cases} \tag{2}$$

Acknowledgements The authors gratefully acknowledge the BLM-Group support in the realization of laser-cut elements. The second and fifth authors acknowledge the Italian Ministry of Education, Universities, and Research (MUR) in the framework of the project DICAM-EXC (Departments of Excellence 2023–2027, grant L232/2016). Finally, the authors acknowledge the laboratory staff at the University of Trento for their precious assistance.

Author Contributions H. N. Olmez: Writing — original draft, Validation, Software, Methodology, Conceptualization, Visualization. T. Guner: Writing — original draft, Writing — review and editing, Methodology, Software, Conceptualization, Visualization. G. Zanon: Writing — review and editing, Methodology, Supervision, Resources, Funding. M. Brugnolli: Supervision, Investigation, Resources, Funding. O.S. Bursi: Writing — review and editing, Methodology, Supervision, Resources, Funding.

Funding Open access funding provided by Università degli Studi di Trento within the CRUI-CARE Agreement.

Data Availability The experimental data supporting the findings of this study, including raw infrared thermography measurements, XRD residual stress data, surface roughness and hardness profiles, and the associated processed datasets are not publicly accessible but can be obtained from the corresponding author upon request.

Declarations

Competing interests This work was conducted in collaboration with BLM-Group. Fourth author is employed by the company. All analyses and interpretations were carried out independently, and the authors declare no other competing interests.

References

1. Chau MQ (2019) An overview study on the laser technology and applications in the mechanical and machine manufacturing industry. J Mech Eng Res Dev 42(5):16–20
2. Shin JS, Oh SY, Park H, Chung C-M, Seon S, Kim T-S, Lee L, Choi B-S, Moon J-K (2017) High-speed fiber laser cutting of thick stainless steel for dismantling tasks. Optics & Laser Technology 94:244–247
3. Kanyilmaz A (2019) The problematic nature of steel hollow section joint fabrication, and a remedy using laser cutting technology: A review of research, applications, opportunities. Eng Struct 183:1027–1048
4. Khatak P et al (2022) Laser cutting technique: A literature review. Materials Today Proceedings 56:2484–2489
5. Mueller S, Kruck B, Baudisch P (2013) Laserorigami: laser-cutting 3d objects. In: Proceedings of the SIGCHI conference on human factors in computing systems, pp 2585–2592
6. Caristan CL (2004) Laser Cutting Guide for Manufacturing. Society of Manufacturing Engineers, Dearborn, MI
7. Execution of steel structures and aluminium structures – Part 1 (2009) Requirements for conformity assessment of structural components
8. EN 1090-2 (2023) Execution of steel structures and aluminium structures – Part 2: Technical requirements for steel structures. CEN
9. Bursi OS, D'Incau M, Zanon G, Raso S, Scardi P (2017) Laser and mechanical cutting effects on the cut-edge properties of steel s355n. J Constr Steel Res 133:181–191
10. Powell J (1993) CO2 Laser Cutting. Springer, London
11. Alsaadawy M, Dewidar M, Said A, Maher I, Shehabeldeen TA (2024) A comprehensive review of studying the influence of laser cutting parameters on surface and kerf quality of metals. The International Journal of Advanced Manufacturing Technology 130(3):1039–1074
12. Eltawahni HA, Hagino M, Benyounis KY, Inoue T, Olabi AG (2012) Effect of co2 laser cutting process parameters on edge quality and operating cost of aisi316l. Opt Laser Technol 44(4):1068–1082. https://doi.org/10.1016/j.optlastec.2011.10.008
13. Genna S, Menna E, Rubino G, Tagliaferri V (2020) Experimental investigation of industrial laser cutting: The effect of the material selection and the process parameters on the kerf quality. Appl Sci 10(14):4956
14. Wang J (2000) An experimental analysis and optimisation of the co2 laser cutting process for metallic coated sheet steels. The International Journal of Advanced Manufacturing Technology 16:334–340
15. Jebbari N, Jebari MM, Saadallah F, Tarrats-Saugnac A, Longuemard J-P (2008) Thermal affected zone obtained in machining steel xc42 by high-power continuous co2 laser. Opt Laser Technol 40(6):864–873. https://doi.org/10.1016/j.optlastec.2007.11.006
16. Diekhoff P, Sun J, Nitschke-Pagel T, Dilger K (2024) A comparative study of the thermal and mechanical cutting influence on the cut-edge hardness of structural steels s355 and s1100. The International Journal of Advanced Manufacturing Technology 130(11):5951–5964
17. Ji D, Zhang J, Liu Y, Zhang B, Chen X, Li R (2025) Microstructural evolution and fatigue performance of 25crmo4 steel remanufactured by high-speed laser cladding of inconel 625 alloy. International Journal of Fatigue, 109291
18. Arif AFM, Yilbas BS, Abdul Aleem BJ (2009) Laser cutting of thick sheet metals: Residual stress analysis. Opt Laser Technol 41(3):224–232. https://doi.org/10.1016/j.optlastec.2008.07.006
19. La Monaca A, Murray JW, Liao Z, Speidel A, Robles-Linares JA, Axinte DA, Hardy MC, Clare AT (2021) Surface integrity in metal machining-part ii: Functional performance. Int J Mach Tools Manuf 164:103718
20. Zanon G, Bursi OS, Scardi P, D'incau M, Raso S (2017) 09.02: Effects of laser cutting on the cut-edge properties of structural steel s355n subjected to high-cycle fatigue. ce/papers 1(2-3):2359–2367

21. Chen C, Gao M, Zeng X (2016) Relationship between temperature at cut front edge and kerf quality in fiber laser cutting of al-cu aluminum alloy. Int J Mach Tools Manuf 109:58–64
22. Yilbas B (2004) Laser cutting quality assessment and thermal efficiency analysis. J Mater Process Technol 155:2106–2115
23. Dubey A, Norkey G, Agrawal S (2012) Parameter optimisation in laser cutting of aluminium alloy sheet. Int J Mechatron Manuf Syst 5(3/4):179. https://doi.org/10.1504/ijmms.2012.048227
24. Miraoui I, Boujelbene M, Bayraktar E (2013) Effects of laser cutting main parameters on microhardness and microstructure changes of stainless steel. Adv Mater Res 664:811–816. https://doi.org/10.4028/www.scientific.net/amr.664.811
25. Rajaram N, Sheikh-Ahmad J, Cheraghi S (2003) Co2 laser cut quality of 4130 steel. Int J Mach Tools Manuf 43(4):351–358
26. Aloke R, Girish V, Scrutton R, Molian P (1997) A model for prediction of dimensional tolerances of laser cut holes in mild steel thin plates. Int J Mach Tools Manuf 37(8):1069–1078
27. Nabavi SF, Farshidianfar A, Dalir H (2024) An applicable review on recent laser beam cutting process characteristics modeling: Geometrical, metallurgical, mechanical, and defect. Int J Adv Manuf Technol 130(5):2159–2217
28. Signer M, Ion A, Sorkine-Hornung O (2021) Developable metamaterials: Mass-fabricable metamaterials by laser-cutting elastic structures. In: Proceedings of the 2021 CHI conference on human factors in computing systems, pp 1–13
29. Mizzi L, Salvati E, Spaggiari A, Tan J-C, Korsunsky AM (2020) Highly stretchable two-dimensional auxetic metamaterial sheets fabricated via direct-laser cutting. Int J Mech Sci 167:105242
30. Yang Q, Li Z, Hao H, Chen W (2023) Compressive mechanical properties and dynamic behaviour of origami-inspired tri-directional auxetic metastructure. Eng Struct 281:115751
31. Luo C, Han CZ, Zhang XY, Zhang XG, Ren X, Xie YM (2021) Design, manufacturing and applications of auxetic tubular structures: A review. Thin-Walled Structures 163:107682
32. Gomes RA, Oliveira LA, Francisco MB, Gomes GF (2023) Tubular auxetic structures: A review. Thin-Walled Structures 188:110850
33. Shu X, Mao Y, Lei M, Da D, Hou S, Zhang P (2022) Toughness enhancement of honeycomb lattice structures through heterogeneous design. Materials & Design 217:110604
34. Sealy MP, Madireddy G, Williams RE, Rao P, Toursangsaraki M (2018) Hybrid processes in additive manufacturing. J Manuf Sci Eng 140(6):060801
35. Kechagias JD, Ninikas K, Petousis M, Vidakis N (2022) Laser cutting of 3d printed acrylonitrile butadiene styrene plates for dimensional and surface roughness optimization. Int J Adv Manuf Technol, pp 1–15
36. Chen K, Yao YL, Modi V (2001) Gas dynamic effects on laser cut quality. J Manuf Process 3(1):38–49
37. Thomas DJ (2011) The influence of the laser and plasma traverse cutting speed process parameter on the cut-edge characteristics and durability of yellow goods vehicle applications. J Manuf Process 13(2):120–132
38. International Organization for Standardization (2017) ISO 9013:2017: Thermal cutting — Classification of thermal cuts — Geometrical product specification and quality tolerances. https://www.iso.org/standard/66548.html. Accessed 02 June 2025
39. Wu S, Wang D, Di X, Li C, Zhang Z, Zhou Z, Liu X (2019) Strength-toughness improvement of martensite-austenite dual phase deposited metals after austenite reversed treatment with short holding time. Mater Sci Eng, A 755:57–65
40. Wen C-D (2010) Investigation of steel emissivity behaviors: Examination of multispectral radiation thermometry (mrt) emissivity models. Int J Heat Mass Transf 53(9–10):2035–2043
41. Noyan IC, Cohen JB (2013) Residual Stress: Measurement by Diffraction and Interpretation. Springer, New York
42. ASTM International (2020) Standard Test Method for Residual Stress Measurement by X-Ray Diffraction for Bearing Steels. Accessed 24 Aug 2025. https://www.astm.org/e2860-20.html
43. ASTM International (2022) Standard Practice for Verifying the Alignment of X-Ray Diffraction Instruments for Residual Stress Measurement. Accessed 24 Aug 2025. https://www.astm.org/Standards/e915.htm
44. Scardi P (2008) Microstructural properties: Lattice defects and domain size effects. In: Powder Diffraction: Theory and Practice, pp 376–412. The Royal Society of Chemistry. https://doi.org/10.1039/9781847558237-00376
45. Taylor D, Clancy O (1991) The fatigue performance of machined surfaces. Fatigue & Fracture of Engineering Materials & Structures 14(2–3):329–336
46. Zhu X, Dong Z, Zhang Y, Cheng Z (2021) Fatigue life prediction of machined specimens with the consideration of surface roughness. Materials 14(18):5420
47. International Organization for Standardization -07-02 ISO 6507-1:2018 – Metallic materials — Vickers hardness test — Part 1: Test method. https://www.iso.org/standard/72198.html. Accessed 02 June 2025